Understanding millennial-scale climate change with simple dynamical systems

Jonathan Melcher* and Sune Halkjær†
PICE, Niels Bohr Institute, University of Copenhagen
(Dated: February 9, 2023)

Since the recognition of abrupt jumps from a cold stadial state to a warm interstadial state by Dansgaard et al. 1993, called Dansgaard-Oeschger (DO) events, attempts have been made to model these as tipping points in a simple dynamical system model. (Berglund Nils 2010; Kowalczyk and Glendinning 2011; Mitsui and Crucifix 2017; Vettoretti et al. 2022). Using a similar formulation for the Stommel model as in Vettoretti et al. 2022 (box-model), we attempt to fit model runs to the ice core behaviour (Rasmussen et al. 2014). We describe the ice core behaviour as the number of warming events (E) and proportion of time spent in stadial conditions (P) as in Lohmann and Ditlevsen 2018. This shows the behaviour of the last glacial; emulating this is the end goal of this project. First, we try to fit the mean structure of the whole glacial with the box-model. We find a strong second-order polynomial correlation between the model averages μ'_E and μ'_P. This arch stands above the measured, μ_E and μ_P, and shows that the box-model is insufficient in achieving the average behaviour of the ice core record. Therefore, we propose a novel model, with a sloping nullcline as opposed to the constant previously used (slope-model). This breaks the second order correlation allowing us to achieve the average underlying processes of event frequency and stadial proportion found in data. We then try to introduce outside forcing in the form of a mix between CO_2 and summer insolation at 65° N. As climate systems are highly complex, a simple model as the box-model, even after the addition of a slope and forcing, struggles in converging to any predictions. Our current best guess shows that both models struggle with capturing marine isotope stage (MIS) 3 and overall needs are higher prevalence of DO events. The absence of declining AMOC strength in interstadial periods in the sloping model does suggest a favouring of the model without slope. We finish by proposing further model changes and showing first steps in implementing further complexity.

"Free convection between two interconnected reservoirs, due to density differences maintained by heat and salt transfer to the reservoirs, is shown to occur sometimes in two different stable regimes, and may possibly analogous to certain features of the oseanic circulation." - Stommel 1961 [a]

[a] We applaud Stommel's beautiful one-sentence abstract and recognise our gluttony.

* KuID: xfk351, Email: jonathan.melcher@nbi.ku.dk
† KuID: tsk420, Email: sune.halkier@nbi.ku.dk

CONTENTS

I. INTRODUCTION

Looking at ice core records from the past glacial periods, abrupt changes in temperature and climate conditions over the northern ice sheets are evident in the proxy data (Dansgaard et al. 1993; Rasmussen et al. 2014). In and around the geographical area that is now Greenland, the climate tipped from a cold stadial state to a warm interstadial state and back again. These events are called Dansgaard-Oeschger (DO) events, named after their discoverers, Willi Dansgaard and Hans Oeschger (Dansgaard et al. 1993). The DO events in Greenland have been proven to be a global phenomenon linked to the rest of the coupled climate system with wind, precipitation, ocean currents, and temperatures around the globe also changing.(Rohling et al. 2009; Stocker and Johnsen 2003; Buizert et al. 2015; Pedro et al. 2018; Corrick et al. 2020; Svensson et al. 2020; Menviel et al. 2020; Pedro et al. 2022). Since the identification of these abrupt changes in 1993 and their related effects, there has been a great deal of interest in understanding the driving forces behind these rapid oscillations. This gives rise to important questions: Are the DO events the driver of the global changes or an effect of another process? Are the DO events purely driven by noise? How fast does the signal travel from the Artic to Antarctica? How do DO events influence precipitation in the Asian monsoon region? These and many other questions in climate system teleconnections have been attempted answered with varying levels of success. It has even been shown that the current paleo records may not have a sufficiently high resolution to infer causal relationships between events or that the global climate system might be so interconnected that the idea of a linear causal relationship is flawed (Capron et al. 2021).

In an attempt to examine these issues from a different angle global coupled climate system models has been developed. These models have until recently required a large amount of operator control of the North Atlantic climate through artificial freshwater forcing to achieve a DO mimicking cycle (Menviel et al. 2014; Menviel et al. 2020). However unforced DO events were achieved by Guido Vettoretti using the Community Climate System Model 4 (CCSM4) model (Vettoretti and Peltier 2016; Vettoretti and Peltier 2018; Gent et al. 2011). With these improved models, it is now possible to increase the spatiotemporal resolution and get an idea of the climate responses in places where records do not exist or are of too low resolution. This can hopefully help in answering some of the questions in climate teleconnection. The models do come with their own set of problems. They are computationally expensive to run, generate results slowly due to the heavy numeric load, and since they are highly interconnected and include a myriad of parameters, nailing down the principle mechanisms behind DO events is difficult. A simple model for describing the DO events is of interest to find principal mechanisms behind the complex models. Such a model was conceived by Stommel 1961, though not with DO events in mind, as they had not yet been identified. However, climate theoreticians have long tried using this model to describe the DO cycle by assuming a causal relationship between it and the Atlantic Meridional Overturning Circulation (AMOC)(Mitsui and Crucifix 2017; Vettoretti et al. 2022; Riechers et al. 2022). The idea is that the AMOC transports energy from the tropics to the north Atlantic during interstadial conditions. This energy is dissipated from the ocean surface and heats Europe and Greenland. If this energy is not added to the northern Atlantic this will lead to stadial conditions. The AMOC is driven by the thermohaline instability between the north and equatorial Atlantic and Stommel showed that this system is inherently unstable using his box-model formulation (Stommel 1961; Menviel et al. 2020; Vettoretti et al. 2022).

Reconciling these simple models with the full-scale climate models they seem to capture somewhat the same dynamics (Vettoretti et al. 2022). Both the coupled full-scale and the simple models are, however, too regular to capture the non-periodic and chaotic nature seen in ice core records.

This project will focus on further developing the box-model in order to more accurately reproduce the behaviour of DO events as seen in the ice core records with a specific focus on the non-periodicity of observed DO events. The project is structured as follows:

In section II we introduce the data and observations describing the North Atlantic climate, along with the statistical methods we will use to compare the model output with the data.

Section III includes a formulation of a Stommel-type box model (Stommel 1961; Vettoretti et al. 2022). In section IV this model is analysed with dynamical systems theory to get the qualitative behaviours of the model. In

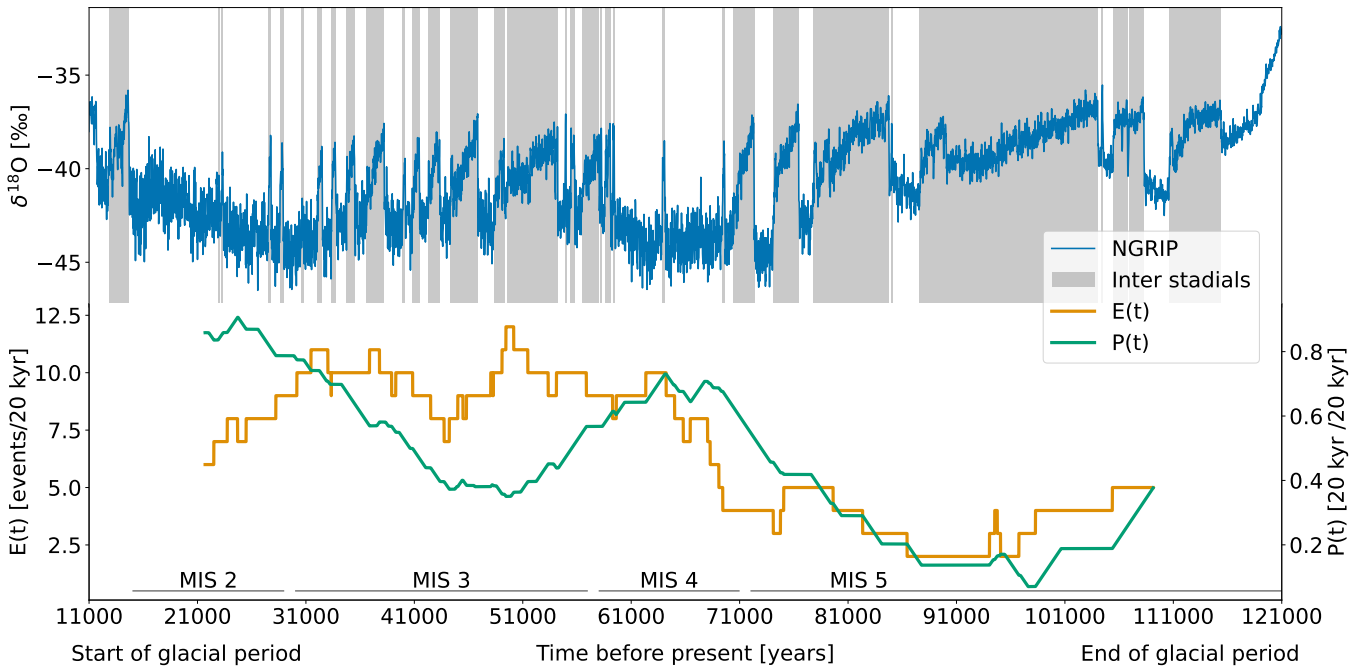

FIG. 1: Analysis of the ice core record. Top: The δ^{18}O record from NGRIP (blue line) with classification of interstadials by Rasmussen et al. 2014. Bottom: The number of events, $E(t)$ (orange), and proportion of time spend in stadial conditions, $P(t)$ (green).

section V we then compare the model with the observations, finding the first model insufficient.

We propose a novel change by introducing a sloping nullcline in section VI, to better match the ice-core data. This new slope-model is analysed with the analytical and numerical tools previously deployed on the initial model. In section VII we try to improve these models even further by introducing external forcing to the model as well. In section VIII we conclude and discuss the advantages of introducing this slope. Following this, an extended *Further works* section explores other additions to the box-model is shown in section IX.

II. DESCRIPTION OF NGRIP DATA AND TIMESERIES ANALYSIS

As mentioned, DO events are recorded in ice cores though water isotypes and dust content. From these records, the warming and cooling events have been classified and synchronized across the NGRIP, GRIP and GISP2 ice cores (Rasmussen et al. 2014). The last glacial period is divided in several time periods, known as Marine isotope stages (MIS). We aim to model the behaviour observed during these periods by constructing statistical methods for comparing our model data with observed data. Here we will introduce the scheme employed by Lohmann and Ditlevsen 2018 and run it on the classification from Rasmussen et al. 2014.

The analysis looks at two statistical parameters to describe the data. The number of warming events in a rolling window, E, and the proportion of time spent in stadial-like conditions, P, again in a rolling window. For E and P the window length is 20 kyr as in Lohmann and Ditlevsen 2018. E is determined by estimating the number of warming events in the window, while for P the number of years in stadial conditions, T_{stadial}, are found and then P is given by $P = T_{\text{stadial}}/(20\text{kyr})$. For the whole timeseries the means, μ_E and μ_P, and uncertainties, δ_E and δ_P, are found. The events to be analysed come from the classification from Rasmussen et al. 2014 excluding the substructure in interstadials where climate drops, but does not reach stadial conditions. We do, however, include GIS-14 from Rasmussen et al. 2014; an interstadial after a small, but (≈150years) long drop in δ^{18}O. This is done to be in line with Lohmann and Ditlevsen 2018. Analysing these events gives the graphs of $E(t)$ and $P(t)$ seen in fig. 1 and μ_E and μ_P found in table I. The mean structure does, however, not seem to

be representative of the overall ice core record, as the MIS 2-5 in the last glaciation give 4 distinct data patterns. First MIS 5 has few but long interstadials, making both $E_{\mathrm{MIS5}}(t)$ and $P_{\mathrm{MIS5}}(t)$ relatively low. Transitioning into MIS 4 there are still few events, but now it is due to long stadials making $P(t)$ increase from 85 kyr. MIS 3 then have more warming events and therefore also a lower proportion of stadials. In the transition to MIS 2 the interstadials become shorter, resulting in an increase in $P(t)$, while also having a low prevalence of events.

Parameter	**Value**
E	(6.577 ± 2.998)events/20 kyr
P	(0.4 ± 0.2)kyr/20 kyr

TABLE I: The results of the analysis of the categorization from Rasmussen et al. 2014.

Having outlined the observations we wish to compare to, we now seek to construct a simple model that can simulate the abrupt changes in the climate.

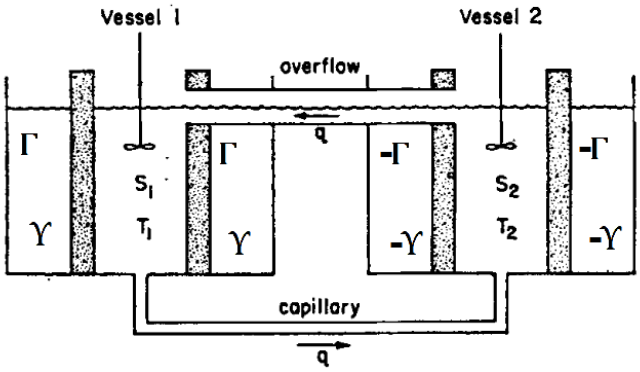

FIG. 2: A double Stommel experiment.Two well-mixed basins of water with temperature, T, and salinity, S, separated by porous walls from a further basin of temperature, Γ and salinity, Υ, connected by a capillary and an overflow to counterbalance the flow from the capillary. Looking at just one vessel and disregarding the overflow and capillary, the experiment reduces to the idealized Stommel model. This is figure 5 from p. 227 in Stommel 1961 with a new name convention added by us.

III. DEFINING THE BOX-MODEL

As our simple model, we have chosen to construct a Stommel-like model as in Vettoretti et al. 2022. The original Stommel model, as described in Stommel 1961, is an idealized representation of the global ocean circulation. It consists of a large vessel filled with water, which is uniformly mixed to ensure a constant salinity (S) and temperature (T) throughout. The vessel is surrounded by porous walls connected to another basin of salinity (Υ) and temperature (Γ), which allow heat and salt to diffuse linearly according to

$$\begin{aligned} \dot{T} &= c(\Gamma - T), \\ \dot{S} &= d(\Upsilon - S), \end{aligned} \tag{1}$$

where c and d are transfer coefficients for temperature and salinity respectively. The dot denotes the time derivative, it will do so for the rest of the project. The idealized vessel can be expanded to a two vessel flow experiment as seen in fig. 2. This experiment now has another basin with porous walls, surrounded by a reservoir of temperature, $-\Gamma$, and salinity, $-\Upsilon$. The two vessels are connected by a bridge for overflow and a capillary for underflow. Driven by salinity and temperature differences, this simulates a region of overturning. The flow, q, going through the capillary is positive when going from vessel 1 to vessel 2, and negative when going from vessel 2 to vessel 1. This flow is counteracted by a flow of equal magnitude going through the overflow, so the volume of the vessels remains constant. Looking for a solution of symmetric form, we define common temperature and salinity as $T = T_1 = -T_2$ and $S = S_1 = -S_2$. Thus, the laws of conservation of temperature and salinity become

$$\begin{aligned} \dot{T} &= c(\Gamma - T) - |2q|\, T, \\ \dot{S} &= d(\Upsilon - S) - |2q|\, S. \end{aligned} \tag{2}$$

Note that the flux is taken as an absolute value, meaning that the system is indifferent to the direction of the circulation. This is nonphysical, as the AMOC is highly directional. However, in our box-model we will be simulating the changes in AMOC strength as a coupled differential equation system, and will thus not be concerned with the direction of the circulation.

The just presented theory is the principle of the multi-vessel Stommel model that is used to make the box-model in Vettoretti et al. 2022. Here we will construct a simple box-model, which we will generalise to represent a northern and a southern box. In fig. 3 we have a South Atlantic

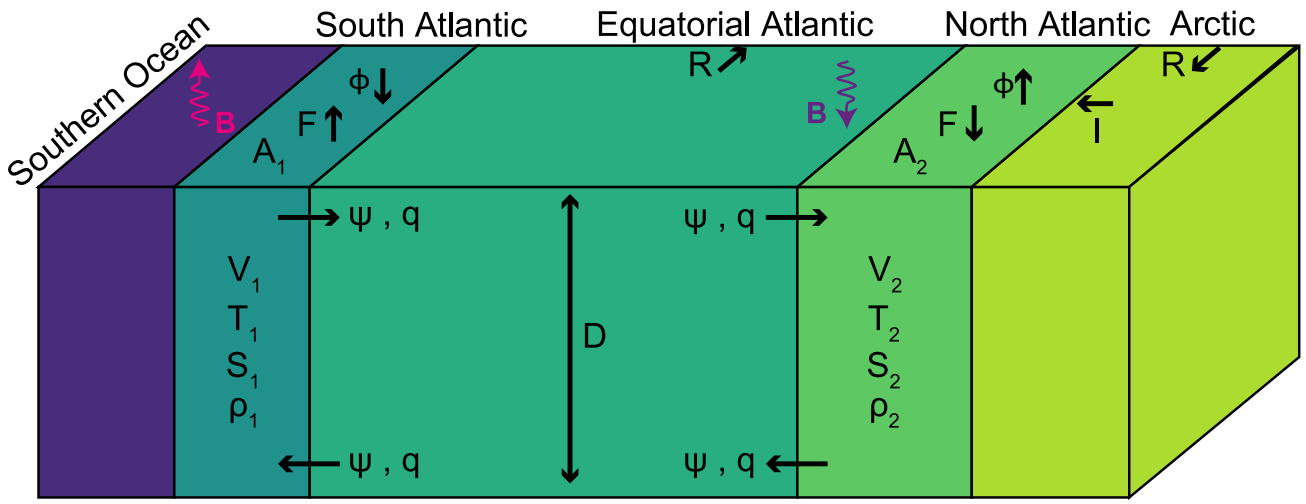

FIG. 3: Box-model of the Atlantic Ocean. The box-model includes variables for volume, V, area, A, pycnocline depth, D, temperature T, salinity, S, density, ρ, heat flux, ϕ, freshwater flux, F, Atlantic-Pacific moisture transport, R, sea ice melt, I, meridional volume transport, ψ, freshwater transport by the AMOC, q, residual buoyancy flux from southern ocean, B, and anomalous buoyancy loss $-B$. In the box-model, the Atlantic-Pacific moisture transport flows out of the Equatorial box and sea ice melt from the Arctic to the North Atlantic is balanced by runoff in the Arctic box, which balances the meridional atmospheric moisture transport from the low-latitude Atlantic to the Pacific and from the south to the north. The residual buoyancy flux is the long-term imbalance of heat and freshwater fluxes absorbed into the Atlantic basins and is assumed to balance the long-term anomalous buoyancy loss along the coast of Antarctica. This is figure S1 from the supplemental for Vettoretti et al. 2022.

box and a North Atlantic box with area $A = A_1 = A_2$ and volume $V = V_1 = V_2$, corresponding to the two vessels in the Stommel model fig. 2. These are in contact with the Southern Ocean and the Arctic respectively, as well as the Equatorial Atlantic and the atmosphere moisture transport. These represent the interacting basins on the other side of the porous walls in fig. 2. The Equatorial Atlantic will also act as the overflow and capillary, as there are surface currents and bottom currents that go in opposite directions (Menviel et al. 2020) We start by considering how an incoming freshwater flux (F) changes the salinity in a basin of salt water. The laws of mass and salt conservation gives,

$$\dot{V} = FA, \tag{3}$$

$$\frac{d(VS)}{dt} = 0 \Rightarrow V\dot{S} = -S\dot{V}. \tag{4}$$

Considering a column of ocean water we can neglect the mass exchange due to salinity change from the freshwater flux caused by evaporation, precipitation, runoff and ice melt as these are of order $1\frac{m}{\text{yr}}$, which is small compared to the average ocean depth (3.7 km). Thus, we will consider S in regards to a reference salinity, S_0, and introduce a "virtual salt flux" per unit area (S_0F). Inserting eq. (3) into eq. (4) leveas us with

$$V\dot{S} = -S\dot{V} = -SFA \approx -S_0FA. \tag{5}$$

For the temperature the law of heat conservation gives,

$$\frac{d(VT)}{dt} = 0 \Rightarrow V\dot{T} = -T\dot{V}. \tag{6}$$

To use this we want to get an expression for $\dot{T}$ in terms of the energyflux into the box. The temperature change in a box is given by

$$\dot{T} = \frac{\dot{Q}}{mc_p}, \tag{7}$$

where $\dot{Q}$ is the energy change in the box and c_p is the specific heat capacity of the box. Multiplying by the volume of the box and defining the heat flux as leaving

the box $\phi = -\dot{Q}A^{-1}$ we get

$$V\dot{T} = \frac{\dot{Q}V}{mc_p} = \frac{\dot{Q}}{\rho c_p} = -\frac{\phi A}{\rho c_p} \tag{8}$$

We can then further express the conservation laws as a set of equations for the temperature and salinity in the South Atlantic and North Atlantic boxes from fig. 3, by taking the temperature and salinity of the flow between them into acount:

$$V\dot{T_1} = -\frac{\phi A}{\rho_0 c_p} - \psi(T_1 - T_2), \tag{9}$$

$$V\dot{T_2} = \frac{\phi A}{\rho_0 c_p} - \psi(T_2 - T_1), \tag{10}$$

$$V\dot{S_1} = -S_0 FA - |q|\,(S_1 - S_2), \tag{11}$$

$$V\dot{S_2} = S_0 FA - |q|\,(S_2 - S_1), \tag{12}$$

where ψ represents the mass/volume transport by the AMOC and q is freshwater transport by the AMOC. The absolute sign arises from indifference in the direction in the two vessel Stommel system.

We will then start reducing the dimensionality of the equations, into a single equation describing buoyancy. First we define meridional temperature change as $\Delta T = T_2 - T_1$, and likewise for density and salinity, $\Delta\rho = \rho_2 - \rho_1$ and $\Delta S = S_2 - S_1$. We will then introduce a linear equation of state for seawater,

$$\frac{\rho}{\rho_0} = 1 + \beta_S(S - S_0) - \alpha_T(T - T_0). \tag{13}$$

This implies

$$\begin{aligned}\frac{\rho_2 - \rho_1}{\rho_0} &= 1 + \beta_S(S_2 - S_0) - \alpha_T(T_2 - T_0) - 1 \\ &\quad - \beta_S(S_1 - S_0) + \alpha_T(T_1 - T_0) \\ &= \beta_S(S_2 - S_1) - \alpha_T(T_2 - T_1), \\ &\Rightarrow \Delta\rho = \rho_0(\beta_S \Delta S - \alpha_T \Delta T),\end{aligned} \tag{14}$$

where T_0, S_0 and ρ_0 are reference values for their respective properties and α_T and β_S are the thermal expansion and haline contraction coefficients. Subtracting eq. (9) from eq. (10), we get the relation for ΔT and ΔS,

$$\begin{aligned}V(\dot{T_2} - \dot{T_1}) &= \frac{2\phi A}{\rho_0 c_p} - 2\psi(T_2 - T_1), \\ V\dot{\Delta T} &= \frac{2\phi A}{\rho_0 c_p} - 2\psi \Delta T.\end{aligned} \tag{15}$$

A similar derivation for salinity can be done using eq. (11) and eq. (12), obtaining,

$$V\dot{\Delta S} = 2FS_0 A - 2|q|\,\Delta S. \tag{16}$$

To further simplify we take the time derivative of density found in eq. (14), remembering that ρ_0, β_S, and α_T are constants,

$$\begin{aligned}V\dot{\Delta\rho} &= V\rho_0 \frac{d}{dt}(\beta_S \Delta S - \alpha_T \Delta T) \\ &= V\rho_0(\beta_S \dot{\Delta S} - \alpha_T \dot{\Delta T}).\end{aligned} \tag{17}$$

We use the time derivative of salinity and temperature from eq. (15) and eq. (16) as well as setting $\psi = |q|$ to allow us to move salt and heat with the freshwater:

$$\begin{aligned}V\dot{\Delta\rho} &= \rho_0 \Big[\beta_S \left(2FS_0 A - 2|q|\,\Delta S\right) \\ &\quad - \alpha_T \left(\frac{2\phi A}{\rho_0 c_p} - 2\psi \Delta T\right) \\ &= 2\rho_0 \big[\beta_S (FS_0 A - |q|\,\Delta S) \\ &\quad - \alpha_T \left(\frac{\phi A}{\rho_0 c_p} - |q|\,\Delta T\right).\end{aligned} \tag{18}$$

While this may not be the most physical representation of the heat and haline flux, it allows us to reduce the number of degrees of freedom in the simple system. Haline flux refers to the movement of salt across two media, usually, two bodies of water or a body of water and the atmosphere. Defining buoyancy as

$$b = -g\frac{\rho - \rho_0}{\rho_0}, \tag{19}$$

we can describe the meridional buoyancy gradient between the southern and northern boxes as

$$\begin{aligned}\Delta b &= b_2 - b_1 \\ &= -g\left(\frac{\rho_2 - \rho_0}{\rho_0}\right) + g\left(\frac{\rho_1 - \rho_0}{\rho_0}\right) \\ &= \frac{-g}{\rho_0}\Delta\rho.\end{aligned} \tag{20}$$

Combining this with eq. (18), we can get the variation in buoyancy,

$$
\begin{aligned}
V\dot{\Delta\rho} &= \rho_0 \left[\beta_S \left(2FS_0A - 2|q|\,\Delta S \right) - \alpha_T \left(\frac{2\phi A}{\rho_0 c_p} - 2\psi \Delta T \right) \right] \\
&= 2\rho_0 \left[\beta_S (FS_0A - |q|\,\Delta S) - \alpha_T \left(\frac{\phi A}{\rho_0 c_p} - |q|\,\Delta T \right) \right], \\
\dot{\Delta b} &= \frac{-2g}{V} \left[\beta_S S_0 F A - \alpha_T \frac{\phi A}{\rho_0 c_p} - |q| \left(\beta_S \Delta S - \alpha_T \Delta T \right) \right].
\end{aligned} \tag{21}
$$

The generalized expression for the total surface buoyancy flux, $B_F + B_H$, is a combination of the haline and thermal forcing derived from the density flux in Schmitt et al. 1989,

$$
\begin{aligned}
F_\rho &= -\rho_0(\alpha F_T - \beta F_S) \\
&= \rho_0 \beta S_0 F - \rho_0 \alpha \frac{\phi}{c_p \rho_0}, \\
B_F + B_H &= -g\beta_S S_0 F + g\alpha_T \frac{\phi}{\rho_0 c_p},
\end{aligned} \tag{22}
$$

where the kinematic fluxes (Wallace and Hobbs 2006) is $F_T = \frac{\phi}{c_p \rho_0}$ and $F_S = S_0 F$ and the density flux has been converted to a buoyancy flux by eq. (20).

Looking at the final term of eq. (21) we can use eq. (20) combined with eq. (14) to get,

$$
\beta_S \Delta S - \alpha_T \Delta T = \frac{\Delta \rho}{\rho_0} = -\frac{\Delta b}{g}. \tag{23}
$$

Using the generalized expression in the time-varying buoyancy, we can simplify eq. (21) to

$$
\dot{\Delta b} = \frac{2}{D}(B_F + B_H) - \frac{2|q|}{V}\Delta b, \tag{24}
$$

where D is the pycnocline depth and the depth of the box fig. 3. From Vettoretti et al. 2022 (found in the supplementary), it is shown that $\frac{2}{D}(B_F + B_H) = -\frac{2B}{D}$, with B as the area-weighted sum of the buoyancy fluxes of the Atlantic Boxes. It also introduces $q = q_0 + \frac{q_1}{b_c}\Delta b$ as a way to relate the simple model to simulations by the CCSM4 model (Vettoretti and Peltier 2016; Vettoretti et al. 2022).

Thus the formulation for the fast timescale becomes,

$$
\dot{\Delta b} = \frac{-2B}{D} - \frac{2}{V}\left| q_0 + \frac{q_1}{b_c}\Delta b \right| \Delta b. \tag{25}
$$

For the slow timescale, we will use an equation with a constant atmospheric CO_2 concentration, γ, as a control parameter. γ is given in units of buoyancy as to function with the rest of the box-model. Temperature is a function of the difference in incoming shortwave radiation and outgoing longwave radiation, which in turn is a function of CO_2 concentration, thereby relating CO_2 concentration to the heat flux, thus justifying the following:

$$
\dot{B} = \frac{F_0}{\tau}(\Delta b - \gamma), \tag{26}
$$

where F_0 is the characteristic haline flux ($[m/s]$). The haline flux in the box-model is an effect of precipitation, evaporation and sea ice melt, causing the concentration of salt in the water to change, at the surface. Alternatively we might use,

$$
\dot{B} = \frac{\kappa_v}{D\tau}(\Delta b - \gamma), \tag{27}
$$

where κ_v is the diapycnal diffusivity ($[m^2/s]$) and the pycnocline depth D ($[m]$) represents ocean vertical mixing. Diapycnal diffusivity refers to the rate at which a substance is mixed or diffused across the different layers of a fluid, in this case, the ocean water. The pycnocline is a layer of the ocean where there is a rapid change in the density.

The AMOC is highly affected by interactions at the ocean surface, resulting in a great influence from precipitation, sea ice melt, runoff and evaporation. Therefore using the surface haline flux F_0 might be favourable. However, when working with the Antarctic Bottom Water (AABW) changes at the surface play less of a role, and looking at the ocean vertical mixing κ_v/D might be more accurate. With values of F_0 and $\frac{\kappa_v}{D}$ chosen here and in Vettoretti et al. 2022 these two equations are very close to being the same, however, different values of κ_v will yield different model outcomes.

The τ in eq. (26) dampens the change in B, causing B to change much slower than Δb, constructing a slow-fast

system. Here one variable changes considerably fast than the other. The normal convention would have a time scale on both eqs. (25) and (26), τ_{fast} and τ_{slow}, where

$$\tau_{slow} \gg \tau_{fast}. \tag{28}$$

However, the same can be achieved with $\tau_{slow} = \tau \gg 1 = \tau_{fast}$, which is how it is implemented in our equations. For numerical analysis, we will need eqs. (25) and (26) in non-dimensional form. Non-dimensional parameters will be expressed as a relative quantity scaled to a characteristic unit and denoted with a prime, for example, $t/t_c = t'$. Expressed in non-dimensional form eqs. (25) and (26) become

$$\frac{d\Delta b'}{dt'} = -B' - \left|q'\right| \Delta b', \tag{29}$$

$$\frac{dB'}{dt'} = \frac{1}{\tau'}(\Delta b' - \gamma'), \tag{30}$$

with

$$t_c = \frac{D}{2F_0};\ q_c = \frac{VF_0}{D};\ B_c = F_0 b_c;\ b_c = \gamma_c, \tag{31}$$

and

$$q' = q'_0 + q'_1 \Delta b'. \tag{32}$$

F_0 can be replaced by κ_v/D in all the characteristics, when changing between the slow eqs. (26) and (27).

The output of our box-model is presented in non-dimensional units, which can be difficult to interpret and relate to real-world phenomena. To make the data more meaningful and easier to understand, we will convert it to an AMOC flow, ψ_{AMOC} in units of Sverdrups (Sv). For the transformation, we will utilise the meridional buoyancy gradient as a scaling factor. The meridional buoyancy gradient refers to the difference in density between different latitudes in the ocean. To relate Δb and ψ_{AMOC} Vettoretti et al. 2022 uses

$$\psi_{AMOC} = \psi_0 + \psi_1 \Delta b, \tag{33}$$

where ψ_0 and ψ_1 are free parameters. To determine these Vettoretti et al. 2022 fits eq. (33), with values of the AMOC strength, ψ_{AMOC} and the buoyancy gradient between the South and North Atlantic box, as modelled by the CCSM4 model and finds the values given in the appendix.

Vettoretti et al. 2022 also introduces a $B_0(\gamma)$ term, which produces horizontal shifts in the slow manifold and a b_0 term, which produces vertical shifts in the manifold. We have chosen to omit the $B_0(\gamma)$ term, as we work with quite sensitive changes in the box-model, and even small shifts with changing γ can prove quite interfering with the stability of the box-model. As the b_0 term is constant, it does not contribute to disruption between model runs and is added to the model. Thus we arrive at the governing equations,

$$\dot{\Delta b} = -B - |q_0 + q_1(\Delta b - b_0)|(\Delta b - b_0), \tag{34}$$

$$\dot{B} = \frac{1}{\tau}(\Delta b - \gamma). \tag{35}$$

Having constructed the governing equations for our simple model, we wish to analyse the theoretical behaviour of the proposed slow-fast system.

IV. SLOW-FAST DYNAMICAL SYSTEMS

The coupled differential equations derived from the box model eqs. (34) and (35) can be analysed using the theory of dynamical systems. In this section, we will introduce slow-fast dynamics, slow manifolds, nullclines, fix points and their stability. Further solutions of stochastic differential equations and the Wiener process will also be introduced. As these concepts are developed they will be applied to eqs. (34) and (35) throughout this section.

A. Analytical analysis

A 2D slow-fast system is a system that contains one fast variable, and one slow: The fast variable is named accordingly as changes in the fast variable will seem virtually instantaneous in the slow variable, and the slow is named accordingly as changes to the slow variable will seem constant in the fast variable as they happen so slowly. In eqs. (34) and (35) the fast variable is Δb and the slow is B as $\tau >> 1$. The slow manifold is defined as everywhere the time derivative of the fast variable is 0 (Berglund Nils 2010; Strogatz 2018; Vettoretti et al.

2022). In our case that is,

$$\dot{\Delta b} = 0 \implies B = -|q_0 + q_1(\Delta b - b_0)|(\Delta b - b_0). \quad (36)$$

This is the yellow, purple and blue line seen in the left panel of fig. 4. The slow manifold cuts the plane in two regimes with different signs of $\dot{\Delta b}$. If the system is above and to the right $\dot{\Delta b} < 0$ and the system moves down to the manifold. On the other side of the manifold, $\dot{\Delta b} > 0$ and the system will moves up to the manifold. If the system reaches a fix point it will stay there as time progresses. Fix points are when the derivative of both variables is 0. For eqs. (34) and (35) this is $\dot{\Delta b} = 0$ and $\dot{B} = 0 \implies \Delta b = \gamma$ represented by the yellow, purple and blue dots on fig. 4. Nullclines are the lines where $\dot{B} = 0$, shown as horizontal lines. The intersect between a nullcline and the slow manifold is a fixpoint. Nullclines also divide the plane into two regimes relating to the $\dot{B}$. If the system is above the nullcline, $\dot{B} > 0$ and vice versa (Berglund Nils 2010; Strogatz 2018; Vettoretti et al. 2022). We will in section VI give the nullcline a slope, making it possible to have multiple fixpoints in a system.

Stability is defined through the system's tendency to diverge or converge to a fixpoint. If the system converges, the fixpoint is stable and if it diverges, it is an unstable fixpoint. Regions of the slow manifold, are called either stable or unstable if a fixpoint in this region would be stable or unstable. Stability is dependent on the eigenvalues, λ_1, λ_2, of the Jacobian matrix for the system, here given by

$$\mathcal{J} = \begin{pmatrix} \frac{\partial \dot{\Delta b}}{\partial \Delta b} & \frac{\partial \dot{B}}{\partial \Delta b} \\ \frac{\partial \dot{\Delta b}}{\partial B} & \frac{\partial \dot{B}}{\partial B} \end{pmatrix}. \quad (37)$$

Many classifications of behaviours have been defined from these eigenvalues for dynamical systems in general. Here we only need the general definitions of stable or unstable fixpoints and bifurcation points. The following is true for fix points and the slow manifold, (Berglund Nils 2010);

- if $\lambda_1, \lambda_2 \in \mathbb{R}$ and $\lambda_1, \lambda_2 < 0$, then it is stable;
- if $\lambda_1, \lambda_2 \in \mathbb{R}$ and $\lambda_i > 0$ for any $i = 1, 2$ then it is unstable;
- if $\mathrm{Im}(\lambda_1), \mathrm{Im}(\lambda_2) \neq 0$ and $\mathrm{Re}(\lambda_1) = \mathrm{Re}(\lambda_2) = 0$ then it is a bifurcation point.

With this we can classify the behaviour of eqs. (34) and (35), determining where there are bifurcations and where the slow manifold is stable. The only non-trivial derivative in $\mathcal{J}$ is,

$$\frac{\partial \dot{\Delta b}}{\partial \Delta b} = -\big|q_0 + q_1(\Delta - b_0)\big| - \Lambda(\Delta b) q_1(\Delta b - b_o), \quad (38)$$

where

$$\Lambda(\Delta b) = \begin{cases} 0 & \text{if } \Delta b = \frac{-q_0}{q_1} + b_0 \\ \mathrm{sign}(q_0 + q_1(\Delta b - b_0)) & \text{otherwise} \end{cases}.$$

The Jacobian thereby end up being

$$\begin{pmatrix} \frac{\partial \dot{\Delta b}}{\partial \Delta b} & \tau^{-1} \\ -1 & 0 \end{pmatrix}. \quad (39)$$

Finding the eigenvalues, $\lambda_{1,2}$, of $\mathcal{J}$ will let us determine the stability of each point on the manifold, fig. 4. We only do this within $\Delta b \in [0.6, 1.58]$. Outside these bounds the manifold does not change stability. Using the definitions outlined above we conclude that, the system for $\Delta b < 1$ is in a stable state since $\lambda_{1,2} < 0$, see right panel of fig. 4. This corresponds to the lower part of the manifold. Then at $\Delta b = 1$, $\lambda_{1,2}$ becomes purely imaginary and the system is undergoing bifurcation. Moving further up, the manifold becomes unstable as $\mathrm{Re}(\lambda_{1,2}) > 0$. Here the system will follow the purple arrows around the slow manifold if not placed perfectly on the fixpoint with no noise. If $\gamma \in]1, \frac{-q_0}{q_1} + b_0[$ this system will always converge to the trajectory shown by the purple lines. This is called the limit cycle. The mathematics of defining limit cycles are beyond this project. Definitions and discussions can be found in Berglund Nils 2010 and Strogatz 2018.

At $b = \frac{-q_0}{q_1} + b_0$ the manifold is non-differentiable and therefore $\mathcal{J}$ is undefined, it can however be shown that a non-smooth bifurcation occurs. Here non-smooth means the absence of the continuous transition from $\mathbb{R}$ to $\mathbb{C}$ to $\mathrm{Re}(\lambda_{1,2}) = 0$ as seen in the lower bifurcation. The mathematics involved in this proof is beyond this project. We have chosen to set $\partial_{\Delta b} \dot{\Delta b} = 0$ to give the desired eigenvalues. For proof of this bifurcation and further discussion see Kowalczyk and Glendinning 2011. After the bifurcation, the manifold is then stable. This is the basis for the classification seen in fig. 4 and much of the further analysis and exploration of this system.

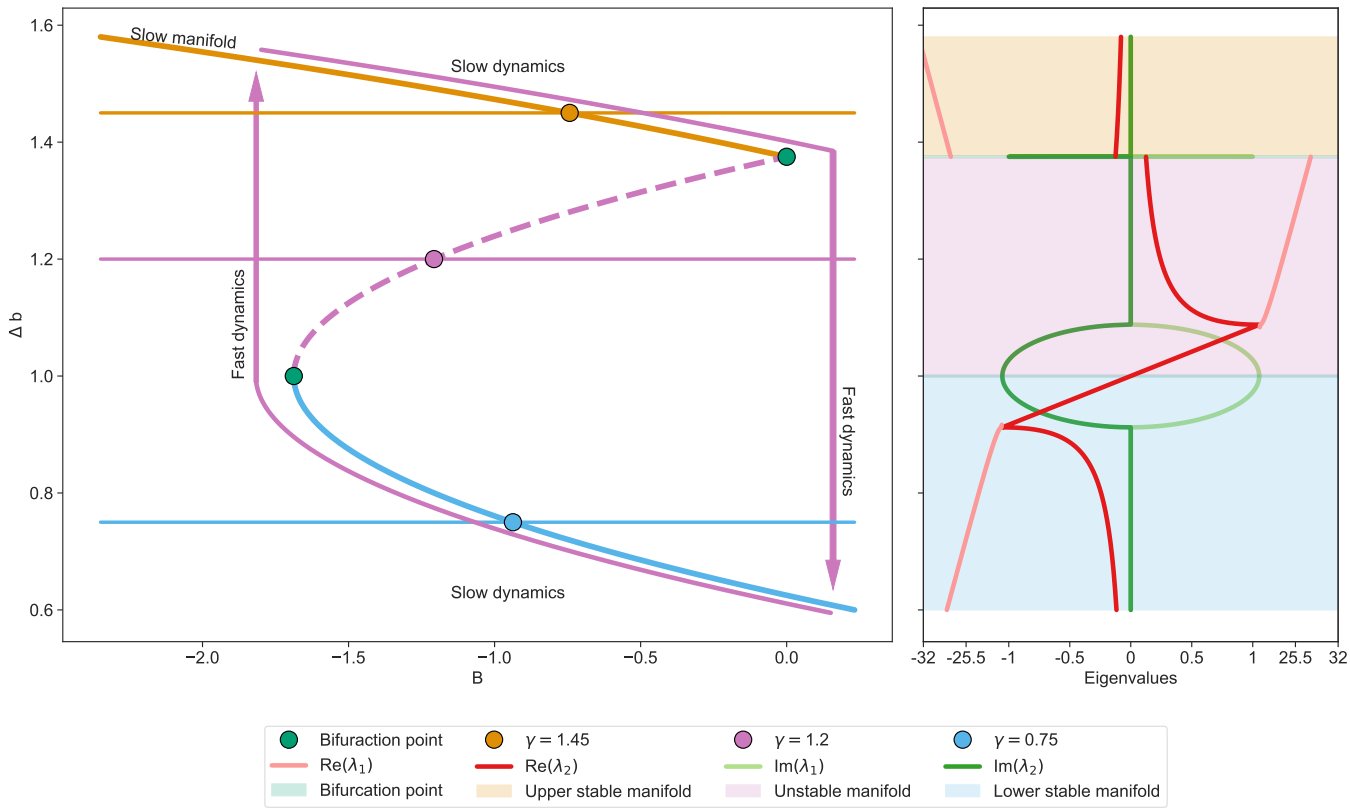

FIG. 4: Stability analysis of the box-model. Left, the slow manifold given by eq. (36) is the S-shaped yellow, purple (dashed) and blue curve. Right, the eigenvalues, $\lambda_{1,2}$, of $\mathcal{J}$, eq. (39), $\mathrm{Re}(\lambda_{1,2})$ in reds and $\mathrm{Im}(\lambda_{1,2})$ in greens. Both plots have Δb on the vertical axis. On the left the yellow and blue circles are stable fix points while the purple is unstable, all made by intersections with nullcline of the same colour. The two green circles are bifurcations. All these points are related to the shaded areas on the right in the corresponding colours. The purple arrows labeled slow- and fast dynamics are the limit cycle of the system.

B. Stochastic systems and defining interstadial onsets

Looking at the NGRIP ice core and weather and climate data in general it is obvious that there is internal variability in all climate systems. To incorporate this internal variability, a Wiener process is added to the model. A Wiener process is a simple stochastic term, dW, added to the ODEs. This term will add a random value drawn from a unit Gaussian to each time step (Berglund Nils 2010; Vettoretti et al. 2022). To control how much noise dominates our system it is multiplied by a control parameter σ, which allows us to control that our system is not purely noise driven. This gives what will from here on be defined as the box-model,

$$\begin{aligned} d\Delta b &= [-B - |q_0 + q_1(\Delta b - b_0)| \\ &\quad (\Delta b - b_0)]dt + \sigma dW \\ dB &= \frac{1}{\tau}(\Delta b - \gamma)dt + \sigma dW. \end{aligned} \tag{40}$$

To numerically solve this system we use the Euler-Maruyama (EM) method, which uses Euler integration to find the next step from the previous step and then adds the Wiener process to each time step. Using EM is not without its consequences as eq. (40) is a stiff system, but by lowering the size of the time step and with the noise in the system, the EM method is stable. The method is favoured for its fast runtime as some experiments require solving the system thousands of times. Finally to be able to test our model runs against the analysis outlined in section II, we need a systematic categorisation of when an interstadial and stadial onset happens. The interstadial onset is defined as the first transition above an upper threshold set to 22 Sv after being below a lower threshold of 11 Sv as in Mitsui and Crucifix 2017. A stadial onset is defined as the reverse process. Understanding the stability of our system and how to model the internal climate variability, we will now solve the system numerically.

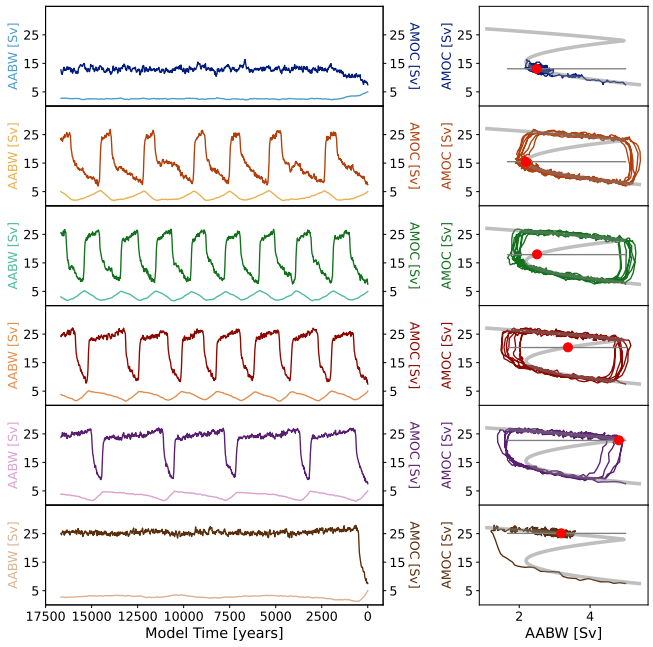

FIG. 5: Box-model simulations. Left: AABW and AMOC as a function of box-model time found from solving eq. (40). Right: The phase space (coloured line) with the slow manifold and nullclines (grey) and the fixpoint (red point) added. Both are shown with increasing $\gamma \in [0.88, 1.48]$. It is evident that for some values of γ, the system is stuck to the lower or upper part of the manifold. However, if the fixpoint is in or close to the unstable part of the manifold then the box-model exhibit periodic oscillations.

V. RESULTS FOR BOX-MODEL RUNS

In section II we introduced the features in the ice core record that we want to model. We will now run the box-model in different configurations and compare it to the ice core record. At first, runs mimicking the results from Vettoretti et al. 2022 will be shown. Then the statistics to compare box-model and data will be introduced. This will be used to make a grid search for the optimal fit to μ_E and μ_P. Lastly, we will discuss the box-model validity focusing on the grid search and the periodicity.

With configurations similar to Vettoretti et al. 2022 we get similar results, as expected. Numerical implementation of eq. (40) shows warming and cooling events mimicking a DO cycle-like behaviour, seen in fig. 5. For γ levels sufficiently below or above, the bifurcation points shown in fig. 4 the box-model is stuck in either interstadial or stadial conditions. If γ is closer to or in the unstable part of the manifold, the box-model exhibit periodic warming and cooling events. Similarly to Vettoretti et al. 2022 we get that γ is a control parameter for the amount of warming events and time spent in interstadial conditions.

Looking at the Antarctic Bottom Water (AABW), lighter colours in left panels of fig. 5, it increases in strength during interstadial conditions and vice versa in stadial. Since AABW is driven by cool freshwater upwelling near Antarctica, a strengthening of this flow leads to a cooling of Antarctica. This is in line with the theorised bipolar seesaw where the signal in the Antarctic ice core is seen as an integrated signal from the AMOC (Stocker and Johnsen 2003; Buizert et al. 2015; Pedro et al. 2018; Svensson et al. 2020). It is also evident that the effect γ has on the AMOC also manifests in AABW with long gradual slow downs and fast uptakes coinciding with low γ and short interstadials and of course fast slowdowns and slow uptakes coinciding with high γ and long interstadials. Further analysis of the AABW is beyond the scope of this project.

We now want to find the optimal parameters for modelling μ_E and δ_P, and a slightly modified χ^2 test is performed, where the uncertainty on the measured values are also included,

$$\chi^2 = \frac{\left(\mu_P - \mu_P'\right)^2}{\delta_P^2 + {\delta_P'}^2} + \frac{\left(\mu_E - \mu_E'\right)^2}{\delta_E^2 + {\delta_E'}^2}, \tag{41}$$

where primed values are simulated and non-primed are measured, this convention is also for $E'(t)$ (simulated) and $E(t)$ (measured) and so on. This notation is kept from here on. To find the minimum of χ^2 we will perform a grid search. From the analytical stability, it is evident that for the box-model to exhibit tipping behaviour γ has to be in the unstable part of the slow manifold. The noise makes it possible to have noise-induced tipping even though the nullcline intersects in the stable part of the slow manifold as long as it is sufficiently close to the unstable part. To avoid the system being purely noise we chose a max value of $\sigma = 0.3$. This sets a bound on how far γ can be from the unstable parts of the manifold before the model stops oscillating. The relevant parameter space is therefore $\sigma \in [0; 0.3]$ and $\gamma \in [0.6; 1.5]$. For each grid point, a Monte Carlo sampling with 20 runs is performed. This gives 20 values for μ_E', μ_P', δ_E', and δ_P' for each point. These are then combined into a single num-

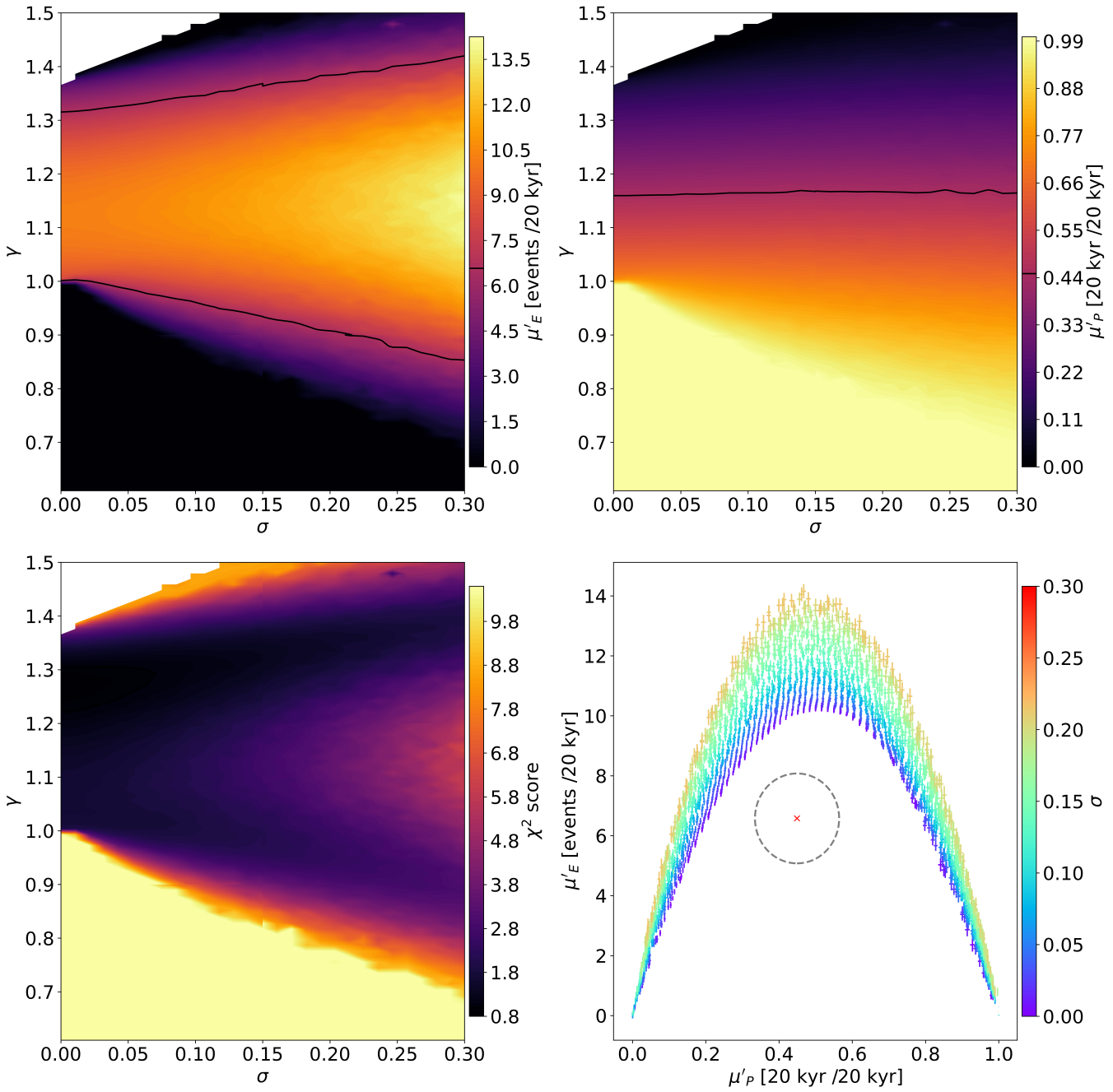

FIG. 6: Monte Carlo grid search of γ and σ. Top left and top right: μ_E and μ_P with contour of the values found in section II. $\mu_E = 6.56$ and $\mu_P = 0.4$ is added as a solid black contour representing the measured values, the optimal parameters are near both. Lower left: The combined χ^2 score as given by eq. (41). Lower right: A scatter plot of μ_E and μ_P, with an ellipse of 1 standard deviation distance (dotted gray) from the ice core record values (0.4,6.56) the red cross. Each pair is colored in accordance to the value of σ used in the corresponding model run.

ber for each grid point by taking a weighted mean, with the weights being the standard deviation. Using eq. (41) each point's mean run is compared to the data, giving a χ^2 value for all. The results of the grid search can be seen in fig. 6. μ'_E is in the phase space distributed as a hill, topping with γ around 1.1, as expected as this value lies in the unstable region of the manifold. With more noise, the number of events also goes up as it is more likely for the system to do a noise-induced tipping point earlier on the slow manifold. The proportion of time spent in stadial conditions is dependent on the level of the nullcline, as also found by Vettoretti et al. 2022. It is indepen-

dent of the noise in the system. The χ^2 is minimised at $\chi^2 = 0.26$, but a large area of the plot can obtain this value. This area has the nullcline to both the upper and lower bifurcation point with σ spanning the whole of the parameter range. This large area is due to the relatively poor precision of the values coming from table I, making the cost of deviating from the true value rather small. This suggests that for a large range of parameters, the box-model can capture μ_E and μ_P.

A scatter plot of each pair of μ'_E and μ'_P found in the grid search with δ'_E and δ'_P as the uncertainties are shown in the lower right panel of fig. 6. It shows that the pairs are clearly correlated with a second order polynomial correlation. These form an arch above the measured μ_E and μ_P, drawn with an oval of one standard deviation around it. The measured values are clearly outside the oval. The data points that are the closest have the lowest σ, and therefore we do not expect that values outside the searched parameter space can come nearer the data than the simulations shown here. Since if we run the simulation with $\sigma > 0.3$ it will be further out in the distribution and if we look for $\gamma \notin [0.6, 1.5]$ the system will be stuck on the stable part of the manifold.

In spite of the low χ^2, the box-model is, therefore, insufficient when it comes to simulating the measured μ_E and μ_P. To find a model that can exhibit the mean behaviour of the ice core record we propose adding a slope to the nullcline.

VI. SLOPING NULLCLINE

To remove the strong second order polynomial correlation between μ_E and μ_P, lower right panel in fig. 6, we add a slope to the nullcline. The hope is that the inclusion of this parameter lets the model achieve μ_E and μ_P closer to the measured values. Of special interest is the effect of a nullcline that intersects both the upper stable part of the slow manifold and the lower stable part, causing the model to have two stable fix points.

Adding this slope is not without its consequences since at the moment there is no physical representation of what the sloping nullcline represents. Therefore we will not include the AABW from here on since the slow parameter can no longer be dimensionalised to this.

Adding a slope, changes equation eq. (35) to

$$\dot{B} = \frac{F_0}{\tau}(\Delta b + \alpha B - \gamma), \tag{42}$$

with the same non-dimensionalization constants and $\alpha_c = F_0^{-1}$ giving:

$$\dot{B}' = \frac{(\Delta b' + \alpha' B' - \gamma')}{\tau'}. \tag{43}$$

We will omit the primes henceforth. This equation combined with eq. (34) will hereafter be called the slope-model. This will be analysed with the tools developed for the box-model. First, we will do some example runs then we will use the analytical analysis to determine the stability of the manifold. Lastly, we will do a grid search and check if we can fit the mean structure, looking especially at if we managed to break the second-order polynomial relation.

A. Example runs

Analysing the behaviour of the slope is two-fold; we can look at the effect of a constant slope and changing the intercept and we can look at the effect of a constant intersection with the slow manifold and changing the slope of the nullcline. Naturally, we will look at both, and later combine these.

First, we will look at a constant slope while changing the intercept. To get a positive slope, α is taken to be negative, since the nullcline is found from,

$$\dot{B}' = 0 \implies \Delta b = -\alpha' B' + \gamma'. \tag{44}$$

In the left panel of fig. 7, we can see the effect of increasing the intercept, γ, on the system. At first, the system is confined to the lower stable region of the manifold. However, as the intercept is increased, noise-induced jumps from the lower to the upper region of the manifold begin to occur. Eventually, the system becomes purely noise-driven and fluctuates between the two fix points. As the intercept is increased further, the system no longer intersects the lower stable region and becomes stuck in the upper region, with noise-induced jumps to the lower region and around the limit cycle. This is the inverse of the situation observed earlier when

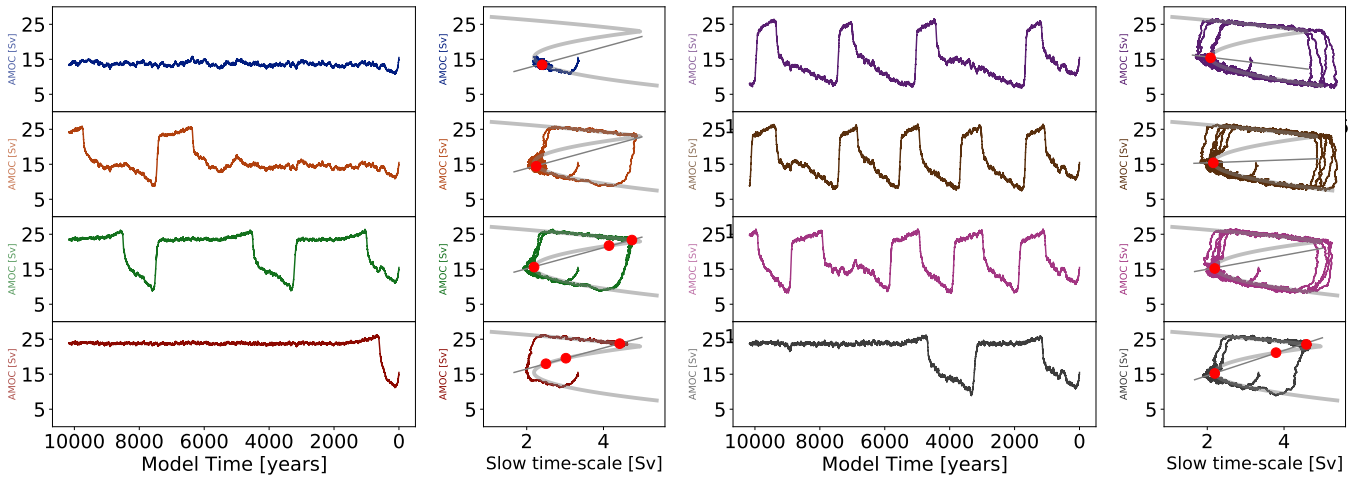

FIG. 7: Slope-model simulation. Left: Slope-model run with fixed $\alpha = -0.25$ and γ going from 1.3 to 1.5. Right: Slope-model run with fixed intersection and α going from 0.1 to -0.3

the system was primarily confined to the lower region.

Now to examine the effect of changing the slope on the system while keeping the intersection with the manifold constant, we will fix the nullcline's intersection at the lower bifurcation point of the slow manifold. This allows us to investigate how the system behaves as the slope is varied and the nullcline approaches and intersects the upper stable region of the manifold. The intercept, γ, is given by the equation $\gamma = \alpha P_x + P_y$, where (P_x, P_y) represent the coordinates of the fix point.

In the right panel of fig. 7, the first three situations show the slope-model being confined to the lower fix point, with noise-induced jumps to the upper manifold and around the limit cycle. In the fourth situation, the slope-model exhibits behavior similar to that seen in situation three of fig. 7, with the system becoming purely noise-driven as the nullcline intersects the slow manifold.

Additionally, we can observe the general effect of the extra term on $\dot{B}$. As α increases, the slope-model exhibits shorter stadial periods and longer interstadial periods, even when the nullcline does not intersect the upper part of the manifold. This demonstrates the influence of the slope on the system's behaviour, even when the intercept is held constant.

B. Stability analysis

We now want to analyse the effect of the added slope on the stability to better understand how it changes the system. This is done to restrict the possible values of α so that a grid search again can be undertaken in a relevant parameter space.

With the added slope on the slope-model, the stability of the system changes tremendously. This is not due to changes in the slow manifold seen in the left panel of fig. 8 as it is not dependent on α. However, B is dependent on α introducing a non-zero entry of the Jacobian compared to eq. (39), resulting in,

$$\mathcal{J} = \begin{pmatrix} \frac{\partial \dot{\Delta b}}{\partial \Delta b} & 1/\tau \\ -1 & \alpha/\tau \end{pmatrix}, \tag{45}$$

where $\partial \dot{\Delta b}/\partial \Delta b$ is given by eq. (38). The stability of the slow manifold is given by the eigenvalues of $\mathcal{J}$, seen for four different slopes in the right panel of fig. 8. α has a multitude of effects on the stability. The biggest change is the disappearance of the bifurcation in the discontinuity given that for $\alpha \neq 0$, $\mathcal{J}$ does not have eigenvalues with zero real part. The eigenvalues as a function of Δb have the same shape but shifted. The imaginary part of the eigenvalues (green lines) is shaped like an oval around 1 and two points at the discontinuity (green points), and increasing the slope moves the oval upwards and moves the two points at the discontinuity closer to 0. Decreasing the slope below $\alpha = 0$ moves the oval down and also moves the discontinues points closer to zero. For the real part of λ_1 (light red) the shape is constant above the discontinuity but the rest of the real parts (both red

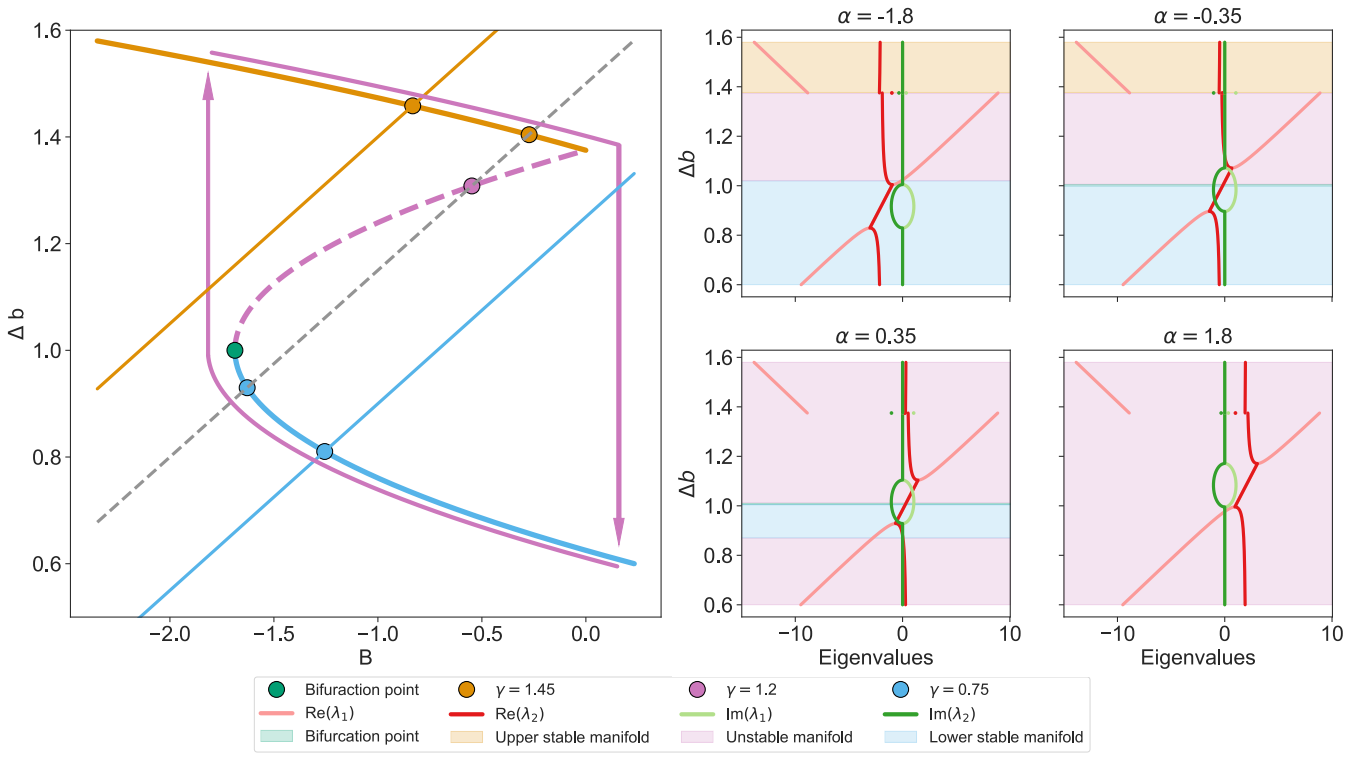

FIG. 8: Analytical stability analysis of the slope-model. Left: Three different configurations of the slope-model with $\alpha = -0.35$, one with a fix point in the interstadial state with $\gamma = 1.75$ (yellow), and one with a fix point in the stadial state $\gamma = 1.25$ (blue), and a configuration with 3 intersects between the nullcline and manifold one in each stability region, $\gamma = 1.5$ (dased grey), this is possible with the addition of a slope. The manifold (S-shaped curve) and limit cycle (purple arrows) is unchanged from fig. 4. Right: Four plots with different α showing the eigenvalues of $\mathcal{J}$. Top left shows a case when there are no longer bifurcations. The top right has the same α as the manifold plot on the left.

lines) moves up and to the right. The movements of the real and imaginary parts combined change the stability of the manifold drastically. For $\alpha = -1.8$ (top left) there are no bifurcation points as $\mathrm{Re}(\lambda_2) < 0$ (dark red line) and the eigenvalues cannot be solely imaginary. At the discontinuity the stability changes from a stable to an unstable fixpoint since $\mathrm{Re}(\lambda_1) > 0$ (light red). Above the oval $\mathrm{Re}(\lambda_1)$ becomes negative again and the manifold is stable. For $\alpha = -0.35$ (top right) the stability is similar to $\alpha = -1.8$, however here there is a bifurcation (green shading) in the imaginary oval above $\Delta b = 1$. For $\alpha = 0.15$ and $\alpha = 0.35$ (bottom row) the stability of the whole manifold changes. The upper and lower parts of the manifold becomes unstable (purple shading) and the system diverges instead of converging to a fix point or the limit cycle. For $\alpha = 0.35$ (lower left) some of the lower manifold is stable (blue shading) but then at around $\Delta b = 0.87$ the real part of λ_2 (dark red) becomes positive, making the manifold unstable. This allows for a half-stable limit cycle where if the system is inside, it converges out to the limit cycle, but if it is outside it diverges. This is a very unstable system as the internal variability will quickly push the system to the outside of the limit cycle. Lastly, for $\alpha = 1.8$ (lower right) $\mathrm{Re}(\lambda_2)$ never becomes negative and no part of the manifold is stable.

This analysis restricts the possible values of α in our analysis to $\alpha \in [-1, 0]$, as for $\alpha > 0$ parts of the manifold becomes unstable with no limit cycle to diverge to and a diverging paleo climate is not physical. The lower bound of $\alpha = -1$ is somewhat arbitrarily chosen to be the point where the lower bifurcation point disappears. We shall see that to fit μ_E and μ_P this is a good bound.

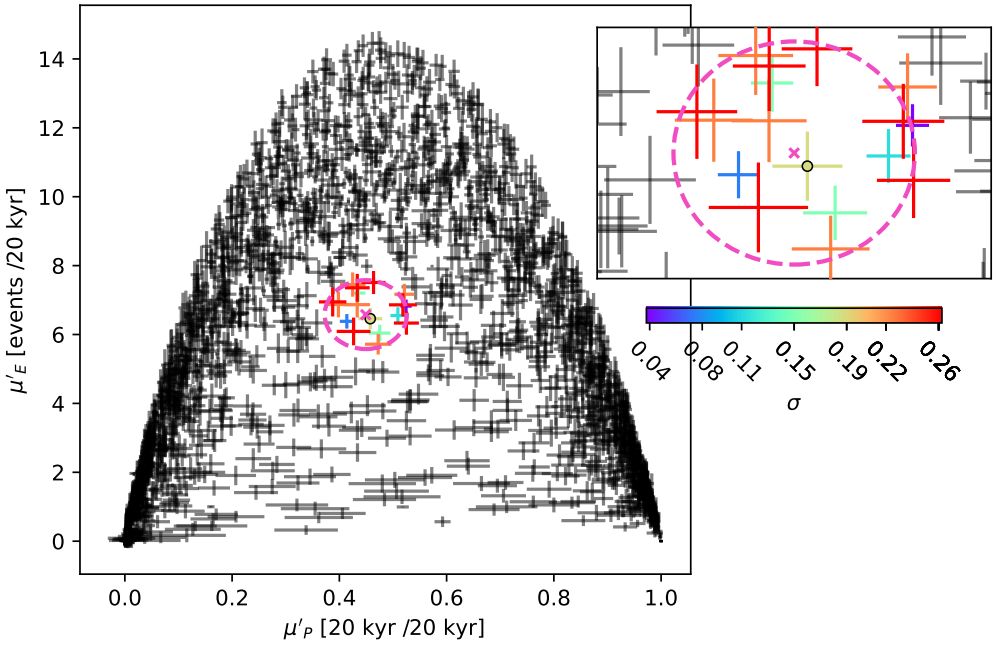

FIG. 9: Achievable μ'_E and μ'_P pairs. Scatter plots of μ'_E and μ'_P pairs from the grid search (black crosses), the error bars are found from the Monte Carlo sampling. With the slope-model is it possible to get within 1 STD (dashed red elipse) of the measured μ_E and μ_P pair (red cross). The 18 μ'_E and μ'_P pairs within 1 STD of the ice record data is coloured depending on the value of σ in the slope-model. The addition of a sloping nullclines makes modelling points inside the sharply defined arch in fig. 6.

C. Numerical analysis

As with the constant nullcline, we will do a grid search and map the χ^2 scores. The parameter space in σ is still $[0, 0.3]$. From the analytical results, we see that $\alpha \in [-1, 0]$ are good bounds and to accommodate the need for larger intersects as the slope increases we set $\gamma \in [0.6, 3]$. In the interest of run time the Monte Carlo sampling has been lowered to 10 runs per grid point.

Fig. 10 shows clearly the constraints the noise has on the system. The lower the noise, the more combinations of α and σ, which will result in the slope-model getting stuck in a fix point. A region of low χ^2 is evident as a v-shape extending to steeper slopes as the noise increases. The minimum of χ^2 is found in this region to be $\chi^2 = 0.0054$ at $\sigma = 0.19 \pm 0.04, \gamma = 1.74 \pm 0.04$, and $\alpha = -0.53 \pm 0.05$, with the uncertainties coming from the resolution of the grid search.

Looking at the scatter plot of μ'_E and μ'_P in fig. 9 it is now possible for the slope-model to simulated pairs close to the measured pair, see the coloured points inside the 1STD dashed line on fig. 9. In contrast to the scatter plot from the box-model, lower right panel of fig. 6, there is no longer a region without values and the strong second order polynomial correlation has disappeared. This permits values close to the means estimated from data and with the closest being the same as the one found with the χ^2 test, marked with a black circle in fig. 9.

To see how this configuration models the last glacial it is run 100 times. The mean $E'(t)$ and $P'(t)$ are found and plotted against the measured $E(t)$ and $P(t)$ see in fig. 11. It is clear that the slope-model captures the mean behaviour very well and is close to the measured value both in μ_E and μ_P. This was impossible with the box-model. It is however also evident that as highlighted in section II the mean structure does not emulate the different MIS's and the transitions between them.

Having shown that adding a slope gives good results concerning the mean behaviour. We now want to simulate the whole glacial with all the different MISs and transitions between them. To attempt this we will introduce a model with outside forcing.

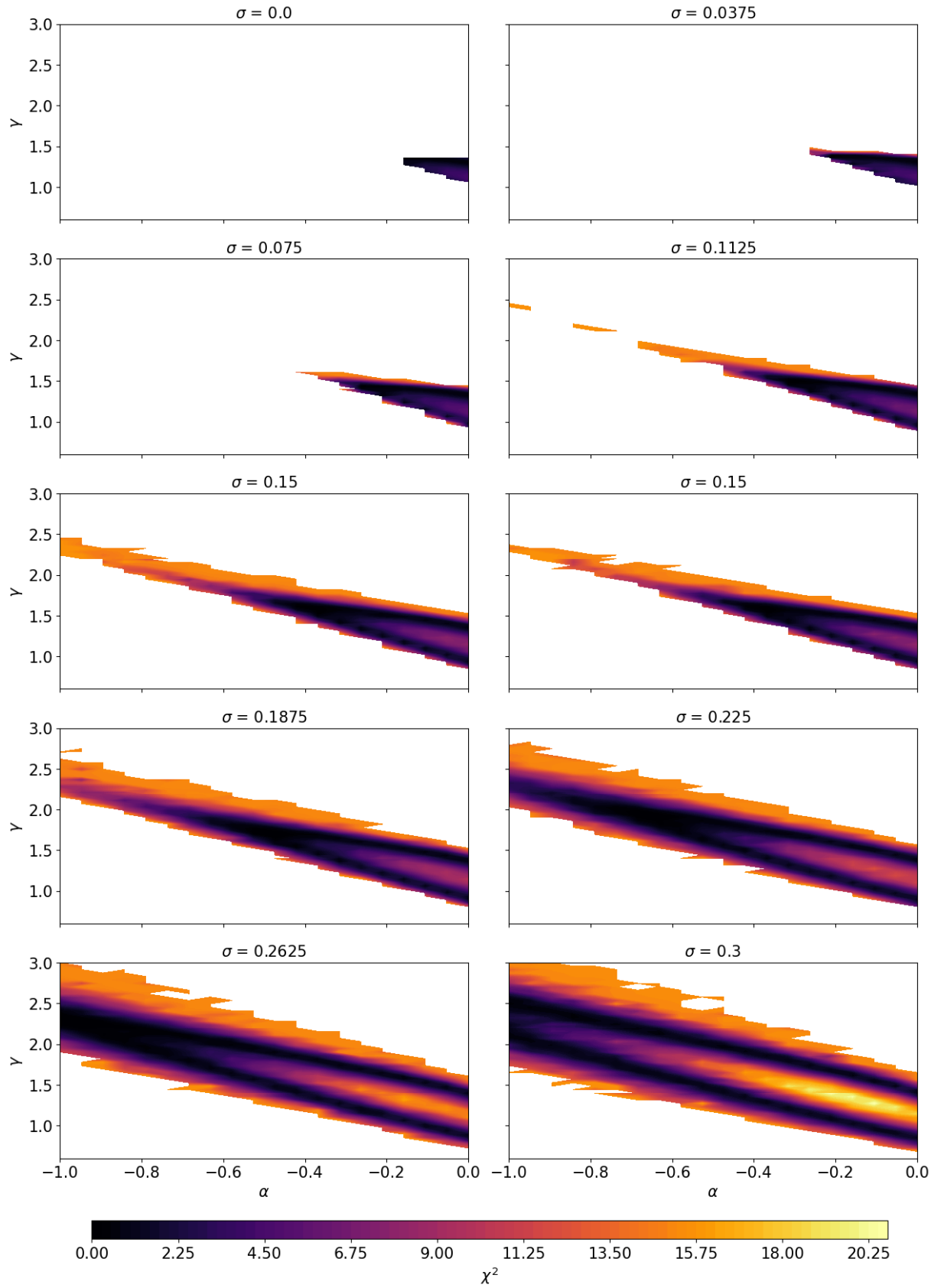

FIG. 10: Gridsearch for the best slope-model configuration. Grids of z-scores as a function of γ, σ, α, with increasing σ for subsequent grids. Since the grid is now 3-dimensional the plots are now slices with constant σ.

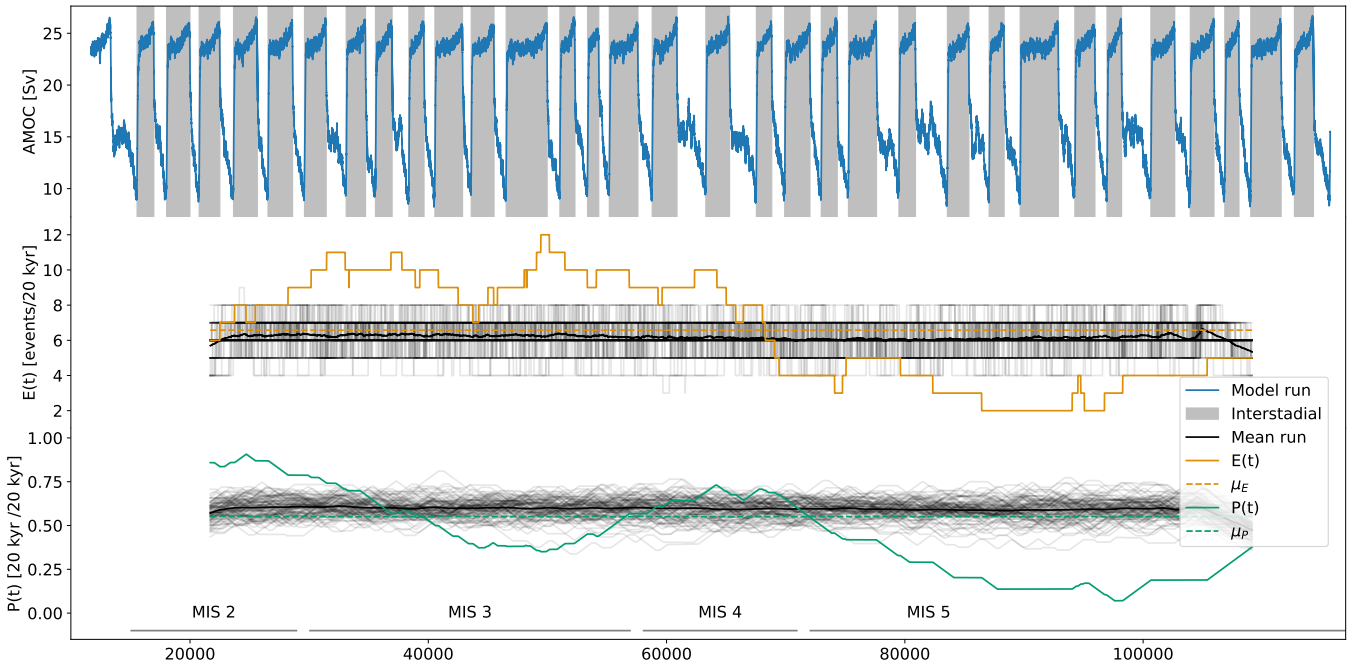

FIG. 11: Best fitting slope-model run. Top: Slope-model run with $\sigma = 0.19 \pm 0.04, \gamma = 1.74 \pm 0.04$, and $\alpha = -0.53 \pm 0.05$ the minimum values found in the grid search. Interstadial periods are marked in grey. Middle: events/20kyr from NGRIP ice core along with the mean (yellow), and from 100 simulation runs (black). Bottom: Propotion of time spent in stadial periods in 20kyr windows from NGRIP ice core along with the mean (green), and from 100 simulation runs (black).

VII. TIME-DEPENDENT NULLCLINE

Up until now, we have run simulations with a static nullcline through time. As we want to work towards applying different kinds of climatic forcing and solar insolation, which is not constant in time, we will investigate the effect of letting the nullcline change throughout time in a model run. Letting the nullcline change through a model run adds another level of complexity to the simulation and allows us to further manipulate stadial/interstadial length and frequency of events.

Before adding the slope to the box-model, the constant nullcline was used to represent different CO_2 levels. While we can not propose a physical representation of the sloping nullcline, we still believe it to be some kind of proxy for a climatic forcing.

We will only have γ changing, but it is possible to have α changing as well. We will implement forcing based on insolation and CO_2, as scaling of the intercept, γ. As we still have no physical representation of α, we also have no way to add an actual data-based time-dependency, thus we will disregard having a changing α in this project.

In fig. 12 we see four different simulations of the box model with an added time dependency on γ, following a defined function. In the first three, we observe similar behaviour to fig. 5; higher γ results in longer interstadials and shorter stadials, and vice versa when γ is low. We can especially see the effect we want to investigate in the parabola and sinusoidal γ runs, where γ rises and falls dynamically, making the frequency and duration of the events change dynamically as well. This is a very powerful tool, as we attain the ability to manipulate the nullcline to produce whichever kind of behaviour we would like; fx. if we want to create a perfect Bond cycle (Bond et al. 1997) we can construct a time evolution of γ, which simulates just this, as seen in the bottom right of fig. 12. In this construction of Bond cycles, it is, however, apparent that the constraints on the changing of the nullcline is quite harsh and probably does not represent anything remotely physical. Thus, the challenge is to find a proper physical forcing which can be implemented to the box-model and the sloping model.

A plethora of external factors have been proposed to force the DO cycles (Mitsui and Crucifix 2017; Lohmann and Ditlevsen 2018; Vettoretti et al. 2022; Riechers et al. 2022). In our project we have chosen to focus on insola-

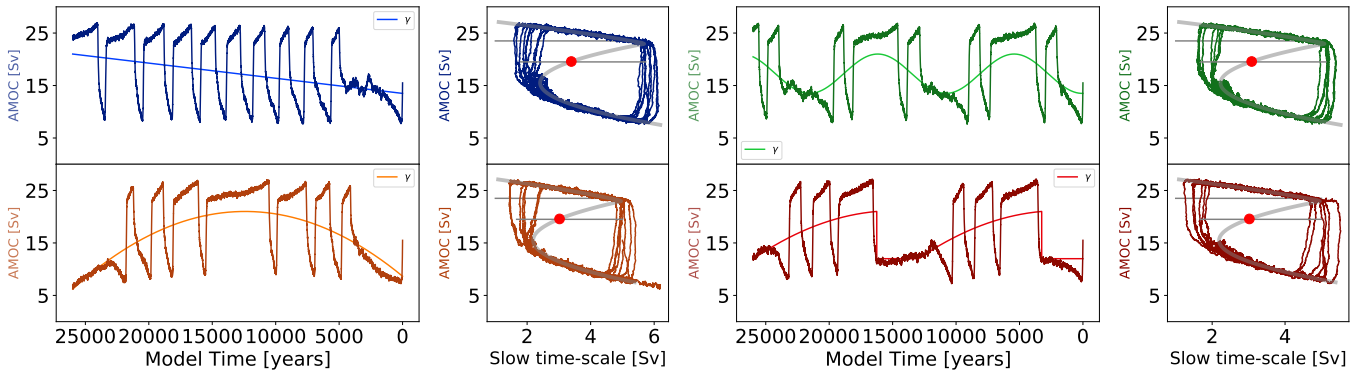

FIG. 12: Box-model runs with time-dependent γ. All four has $\gamma \in [0.9, 1.4]$ Upper left: γ increase linearly. Lower left: γ follows a parabola with peaking at $= 1.4$. Upper right: γ follows sinusoidal function. Lower right: γ constructed to simulate Bond cycle behaviour (Bond et al. 1997).

tion, F_{inso}, and atmospheric CO_2 concentration, F_{CO_2}. F_{inso} is given by the total energy in summer at 65° N from Huybers 2006. F_{CO_2} is given by the combined CO_2 record by Bereiter et al. 2015. To implement this forcing as a divergence from a given mean the data is standardised. This is done by subtracting the mean and dividing by the maximum absolute deviation, giving a series around 0 that maximally deviates from this mean by 1. To combine the two data series they are interpolated, using cubic interpolation, to be on the same time scale as the simulations.

As it is unknown what the optimal mix and strength of the external forcing is the amplitude of the forcing and the mixing of F_{inso} and F_{CO_2} are left as free parameters. Thus the γ used in the simulations is,

$$\gamma = \gamma_0 + A\left[\beta F_{CO_2} + (1-\beta)F_{inso}\right], \tag{46}$$

where γ_0 is a free parameter controlling the mean value, A is the amplitude of the forcing and β is the percentage of forcing being F_{CO_2}. Another parameter is needed as F_{inso} requires a threshold to define summer, S_{off}. We want to analyse the two models when γ is given by eq. (46). To determine whether a simulation is close to the data a sample of 100 runs is made and the mean and uncertainty on the mean of the 100 time-series for $E'(t)$ and $P'(t)$ are found. This is then compared to the measured $E(t)$ and $P(t)$ using a χ^2 test. We want the χ^2-value to be the same size as the number of degrees of freedom, given by

$$N_{dof} = N_{data} - \nu,$$

where $N_{data} = 87437$ and ν is either 4 or 5 for the box- and slope-model respectively.

Due to time constraints in the project, we have not been able to have a fitting routine to converge and we have shown an example found by educated guesses. For the box-model the lowest χ^2-value found is 10^8 using the parameters shown in section VII. This is not close to the desired value of around $N_{dof} \sim 9 \cdot 10^4$, this run is shown in fig. 13). It is clear that the box-model mainly diverges from the data in the number of events in MIS 3. The proportion of time spent in stadials seems to follow the general structure of the real data but is in the χ^2-test also very far from the real value. Looking at the slope-model, the best χ^2-value found is $\chi^2_E = 5 \cdot 10^7$ and $\chi^2_P = 10^7$, using the parameters from section VII. Here $P'(t)$ fits the overall structure but $E'(t)$ seems further off. However, the χ^2-scores are lower for both $E'(t)$ and $P'(t)$ with the slope. We attribute this to a higher variation in the runs leading to larger uncertainties on the mean when run with the same number of experiments. These lower χ^2-values, do not necessarily reflect a better fit but might be caused by this larger variation. Looking purely at the distance between the models and the data in $E'(t)$ the box-model is better at capturing the data. Moreover, the box-model is more dynamic reaching a higher maximum value and lower minimum before MIS3.

It is paramount to find a way to fit the forced models $E'(t)$ and $P'(t)$ to the observed values. We suggest a basin hopping algorithm, as this might avoid the false minimums that stem from the Wiener process. Furthermore, global ice volume should be included in the forcing mix, since global ice volume has been found by Mitsui

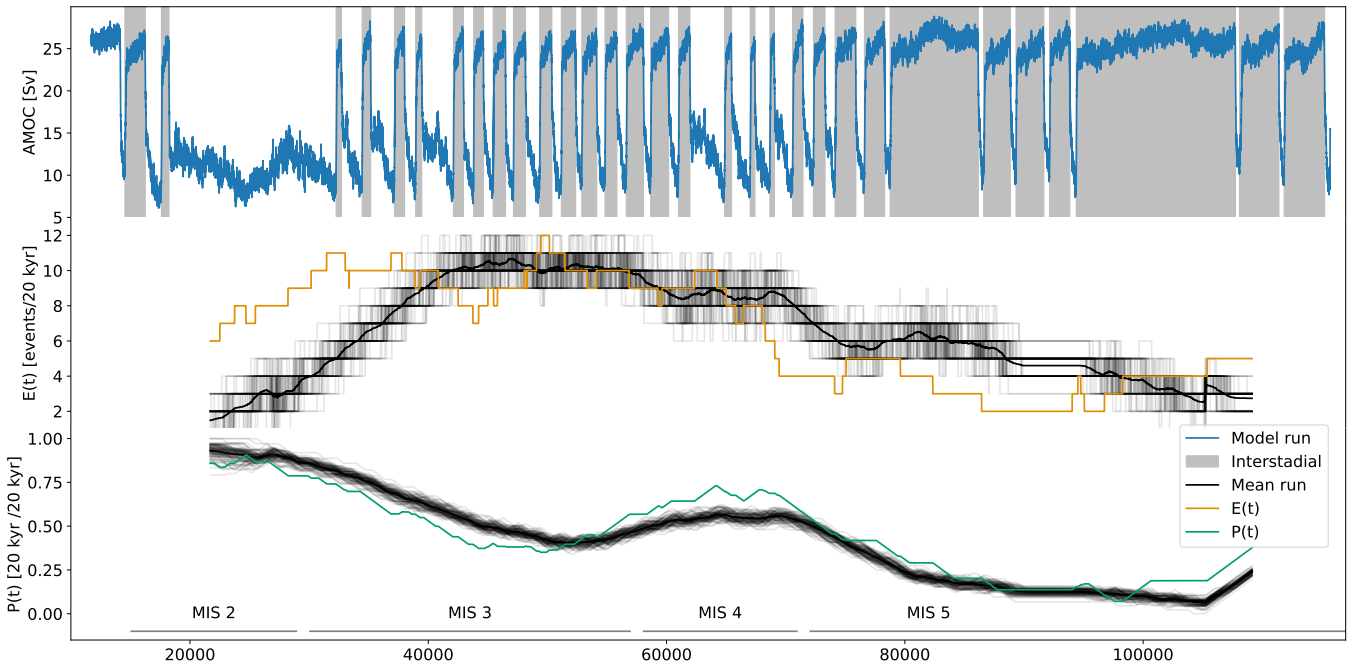

FIG. 13: Glacial simulations using the box-model. Top panel, a single of the 100 sample run using $\gamma = 1.2, \sigma = 0.14, \beta = 0.55$ and $A = 1$, with a summer threshold for F_{inso} of $400W/m^2$. Middle, the black lines are the simulated $E'(t)$ and the yellow the measured $E(t)$. Bottom, the black lines are the simulated $P'(t)$ and the green is the measured $P(t)$. The simulated $P'(t)$ curves follow the structure of the measured values while the simulated $E'(t)$ curves is quite far from the measured, especially around the end of MIS 3.

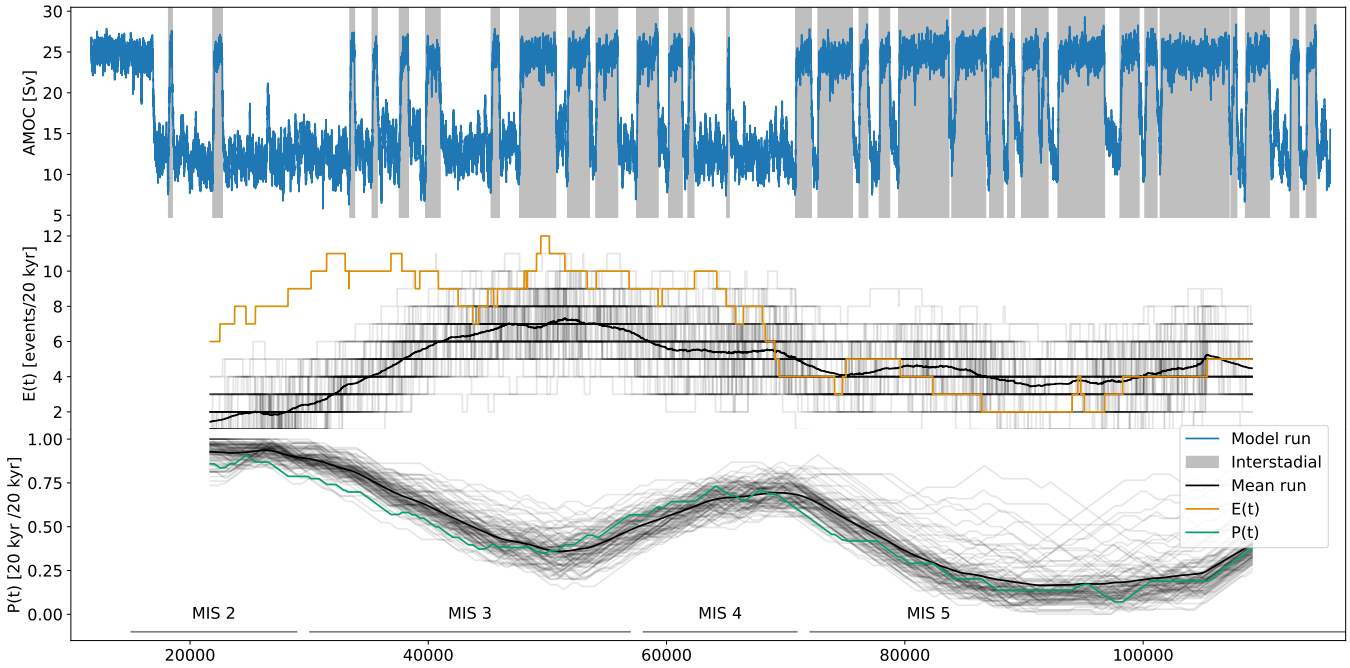

FIG. 14: Glacial simulations using the slope-model Top panel, a single of the 100 sample run using $\gamma = 1.8, \sigma = 0.225, \alpha = -0.58, \beta = 0.45$ and $A = 0.8$, with a summer threshold for F_{inso} of $325W/m^2$. Middle, the black lines are the simulated $E'(t)$ and the yellow the measured $E(t)$. Bottom, the black lines are the simulated $P'(t)$ and the green is the measured $P(t)$. The simulated $P'(t)$ curves follow the structure of the measured values while the simulated $E'(t)$ curves is quite far from the measured.

and Crucifix 2017 to be more dominant compared to atmospheric CO_2 and summer insolation at 65°N.

	Box-model	Slope-model
χ^2_E	10^8	$5 \cdot 10^7$
χ^2_P	10^8	10^7
γ	1.2	1.82
σ	0.14	0.23
β	0.55	0.45
A	1	0.8
S_{off}	$400\frac{\mathrm{W}}{\mathrm{m}^2}$	$325\frac{\mathrm{W}}{\mathrm{m}^2}$
α	n/a	-0.58

TABLE II: The model parameters that give the lowest χ^2-values when compared to $E(t)$ and $P(t)$ from section II.These are found by guessing as a fitting routine could not converge therefore no uncertainties could be estimated.

VIII. DISCUSSION AND CONCLUSION

We set out in an attempt to make a simple model that could simulate the ice core record in the MIS and the transitions between. First, we tried to model the mean structure of the whole record. Here we found that by adding a slope to the nullcline the model improves its ability to simulate the estimated mean behaviour of the ice core record. By adding the slope we were able to obtain values of μ'_E and μ'_P that were closer to the measured values than without a slope. The area under the arch in fig. 6 can only be achieved by the slope-model. As μ_E and μ_P do not accurately represent the MIS structure we then tried to introduce external forcing.

We attempted to simulate the entire ice core record and found that the ability to fit $E(t)$ and $P(t)$ is not necessarily improved by adding a slope. Comparing the best guess for the two models with external forcing shown in section VII, a χ^2-test showed that the sloping nullcline may be a better model, but this could be due to the added variability it brings. It is not clear which model is better because we were unable to get a fit to converge, thus a better set of parameters might exist for both models. As suggested it might be beneficial to look at bassin hopping algorithm to avoid false minimums.

In the forced model runs, it is evident that both models fit the data for $P(t)$ best. There are two main reasons for this: firstly, as shown in the top right panel of fig. 6, there is a strong linear relation between the value of γ and μ'_P. Secondly, the forcing affects γ, and there is a numerically large Pearson correlation coefficient between the chosen forcing and $P(t)$ in the ice core record, at $\rho_{box} = -0.88$ and $\rho_{slope} = -0.84$. Examining $E(t)$, we see that there is no linear relationship between γ and μ'_E in fig. 6, and this relationship is not independent of σ. In the three-dimensional case, this relationship becomes more complex, but not linear. The Pearson correlation coefficient between the combined forcing and $E(t)$ in the ice core record is relatively weak, at $\rho_{box} = -0.54$ and $\rho_{slope} = -0.29$. While both models can achieve good correlation between $E'(t)$ and $E(t)$, reaching a correlation coefficient up to 0.85 for the slope-model with certain parameter values ($\gamma = 1.575, \sigma = 0.139, \alpha = -0.290, \beta = 0.5, A = 0.7$, and $S_{off} = 325\frac{\mathrm{W}}{\mathrm{m}^2}$). These runs (not shown here) are, however, too low in $E'(t)$ and $P'(t)$ and fit poorly with the χ^2-values.

Both models fail to fit the data in MIS 2 and MIS 3. One potential reason for this is the absence of volcanic eruptions in the model. As demonstrated in Lohmann and Svensson 2022, volcanic eruptions are more closely associated with interstadial onsets than would be expected if they were unrelated random processes. There are as mentioned in section I a lot of caveats with timing and the causal relationship between interstadial onsets and other climate events (Capron et al. 2021; Lohmann and Svensson 2022). If we assume that the seven events identified in Lohmann and Svensson 2022 are causing warming events during the period from 10 ka to 60 ka, we can expect an average of three additional events in each time window. This may add another volcanic event during the Last Glacial Maximum, bringing the average number closer to four in this period. This could make up for the difference between modelled and observed $E(t)$. Looking at $P(t)$, these additional events would occur at low γ values, resulting in short DO events that only slightly decrease the modelled $P(t)$. Since the current models have too high of a $P(t)$ at this time, the inclusion of these events may also correct this. One way to incorporate the effects of volcanoes in the model is by adding a large increase in the AMOC or increasing the noise, σ, drastically for a few time steps. This should have a small chance of occurring at each time step, matching the frequency of volcanoes during the last ice age. To see if this frequency is constant throughout the last glaciation we must wait till we have the data set for the whole period. Lohmann and Svensson are currently working on extend-

ing their study to include the Last Glacial Maximum and the period from 60ka to the glacial onset. Another external forcing is global ice volume which has by Mitsui and Crucifix 2017 been shown to be a more dominant forcing than both atmospheric CO_2 and summer insolation, and should therefore also be included in the analysis.

When examining individual interstadials in greater detail, the two proposed models produce different results. In the box-model, fig. 13, there is a gradual weakening of the AMOC and therefore a gradual cooling of the Greenlandic climate, while in the slope-model, fig. 14, the interstadials have a constant AMOC and climate.

The differences between the two models are due to the number and stability of fix points. In fig. 13, with $\gamma = 1.2$, there is only one unstable fix point which causes the model to follow the limit cycle, following the manifold in its entirety and thus having cooling in interstadial and warming in stadials, see purple lines in fig. 4. In fig. 14, with $\gamma = 1.821$ and $\alpha = -0.579$, there are three intersections, two stable and one unstable, fig. 8. As a result, the system follows the slow manifold until it reaches a stable fix point. If the added noise is large enough, it can push the system to the other side of the slow manifold, causing it to follow the limit cycle until it reaches the second stable fix point, where it remains until the noise pushes it around the limit cycle again. When the system is stuck at a fix point, the AMOC and climate conditions are constant and therefor; the model has constant conditions in stadial and interstadial conditions. In the NGRIP record, fig. 1, the δ^{18}O in the interstadials also falls, which does not match the tipping modelled by the box-model with a slope. However, this does not necessarily reject the slope-model, as there are pairs of γ and σ where there is only one stable fix point and sloping interstadials, as shown in fig. 7. Adding the slope to the equations results in an additional term on the slow parameter. α and B are both always negative, resulting in a positive feedback on the slow parameter, making it unintuitive that the interstadials are slowing down. However, the relative increase in the value of γ outweighs the positive feedback from the addition of the slope, though high values of α can shift the feedback. The system will at that point be more affected by the double intersection.

In summary, based on the data and analysis presented, it can be concluded that a box model alone is insufficient for simulating the mean behaviour of the last glacial period. The addition of a slope is necessary to accurately represent the measured μ_E and μ_P. Additionally, the study concludes that to achieve a description of the whole temporal structure of $E(t)$ and $P(t)$, forcing needs to be added to the model. An attempt using CO_2 and solar insolation was set forth, but more work is needed to find the representation of climate forcing.

IX. ADDING COMPLEXITY

This section will explore and explain further ideas, which can be implemented in the box-model to achieve more complexity and possibly more accuracy in the simulations. We show the first steps in implementing and analysing these ideas and discuss the results we expect to evolve from these implementations.

A. Superposition

The box-model (Vettoretti et al. 2022) uses a single equation for the slow timescale dynamics which can be either,

$$\frac{dB}{dt} = \frac{F_0}{\tau}(\Delta b - \gamma), \tag{47}$$

or

$$\frac{dB}{dt} = \frac{\kappa_v}{D\tau}(\Delta b - \gamma). \tag{48}$$

As described in sec. III there is an argument for using the former with increased AMOC strength and the latter with increased AABW strength. Thus it might be more correct to use a weighted effect of both. We will therefore introduce the following equation for the slow timescale:

$$\frac{dB}{dt} = \frac{\Delta b - \gamma}{\tau}\left(\frac{\kappa_v}{D}\frac{b_{int} - \Delta b}{b_{int} - b_{sta}} + F_0\frac{\Delta b - b_{sta}}{b_{int} - b_{sta}}\right), \tag{49}$$

with b_{int} and b_{sta} as bounds for where the system is entirely driven by interstadial or stadial conditions respectively. This can be seen by looking at Δb in the limits $\Delta b \to b_{int}$ and $\Delta b \to b_{sta}$, here eq. (49) reduces to eqs. (47) and (48) respectively.
Rewriting equation eq. (49), and adding the slope, leads

to:

$$\frac{dB}{dt} = F_0 \frac{\Delta b + \alpha B - \gamma}{\tau} \left(\frac{\kappa_v}{DF_0} \frac{b_{int} - \Delta b}{b_{int} - b_{sta}} + \frac{\Delta b - b_{sta}}{b_{int} - b_{sta}} \right). \tag{50}$$

We can introduce the dimensionless size $\zeta = \frac{\kappa_v}{DF_0}$, and the rest of the equation can be non-dimensionalized using the same characteristic values as the original equation and $b_{max,c} = b_{min,c} = b_c$, leading to

$$\frac{dB'}{dt'} = \frac{\Delta b' + \alpha B - \gamma'}{\tau'} \left(\zeta \frac{b'_{max} - \Delta b'}{b'_{max} - b'_{min}} + \frac{\Delta b' - b'_{min}}{b'_{max} - b'_{min}} \right). \tag{51}$$

This model will henceforth be called the superposition-model. Looking at how the stability is affected, this adds another dependency on Δb, changing 2 of the eigenvalues of the Jacobian eq. (37) to

$$\begin{aligned} \frac{d\dot{B}}{d\Delta b} &= \frac{1}{\tau} \left(\zeta \frac{b_{int} - \Delta b}{b_{int} - b_{sta}} + \frac{\Delta b - b_{sta}}{b_{int} - b_{min}} \right) \\ &\quad + (\Delta b + \alpha B - \gamma) \frac{1 - \zeta}{b_{int} - b_{sta}} \\ &= \frac{1}{\tau(b_{int} - b_{sta})} \Big[\zeta(b_{int} - \Delta b) + (\Delta b - b_{sta}) \\ &\quad + (\Delta b + \alpha B - \gamma)(1 - \zeta) \Big], \\ \frac{d\dot{B}}{dB} &= \frac{\alpha}{\tau} \left(\zeta \frac{b_{int} - \Delta b}{b_{int} - b_{sta}} + \frac{\Delta b - b_{sta}}{b_{int} - b_{min}} \right). \end{aligned} \tag{52}$$

This gives rise to several complexities in the stability, as the eigenvalues also become dependent on B. We only want to explore the effects of the superposition. Therefore, we will take α to be 0, as otherwise, the complexity rises beyond the scope of this project. Thus the previous equations become

$$\begin{aligned} \frac{d\dot{B}}{d\Delta b} &= \frac{1}{\tau(b_{int} - b_{sta})} \Big[\zeta(b_{int} - \Delta b) \\ &\quad + (\Delta b - b_{sta}) + (\Delta b - \gamma)(1 - \zeta) \Big], \\ \frac{d\dot{B}}{dB} &= 0. \end{aligned} \tag{53}$$

However as we still have a dependency on γ, we will investigate the effects on the eigenvalues from changes in γ. As $\gamma > 1.6$ and $\gamma < 0.6$ does not provide further interesting model results, we will do a stability analysis as in section IV for fixed γ in the two edge cases, see in fig. 15. Here we have calculated the eigenvalues of both the system with and without superposition and then shown the difference in these, for both values of γ. On the two plots on the right of fig. 15 we can see, that there is a difference in the value of the eigenvalues. However, in the oval region, the difference is solely in the imaginary values and thus does not change the stability of the system. Interestingly enough, while there are differences in the imaginary and real parts of the eigenvalues for different Δb, there is never a difference in both the imaginary and real parts at the same time, only in one or the other.

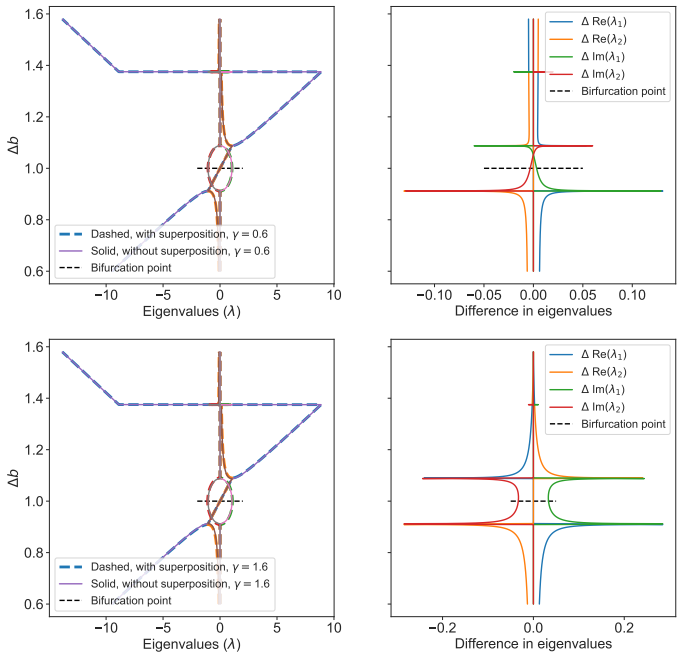

FIG. 15: Stability of the superposition-model Left: Overlayed eigenvalues of the superposition-model for fixed $\gamma = 0.6$ and $\gamma = 1.6$. Dashed lines denote eigenvalues with added superposition, solid lines denote eigenvalues without. Right: Difference in eigenvalues.

Therefore, we will not concern ourselves with the effect of γ going forward. Running the box-model with added superposition, $\gamma = 1.4$ and $\sigma = 0$, for both values of $\kappa_v = 1 \cdot 10^{-4}$ and $\kappa_v = 1 \cdot 10^{-5}$, resulted in the plots shown in fig. 16

Here we first see the minimal difference in using superposition when $\kappa_v = 1 \cdot 10^{-4}$, as the value almost coincides with using F_0. However, lowering κ_v results in longer stadial periods, while preserving the interstadial behaviour.

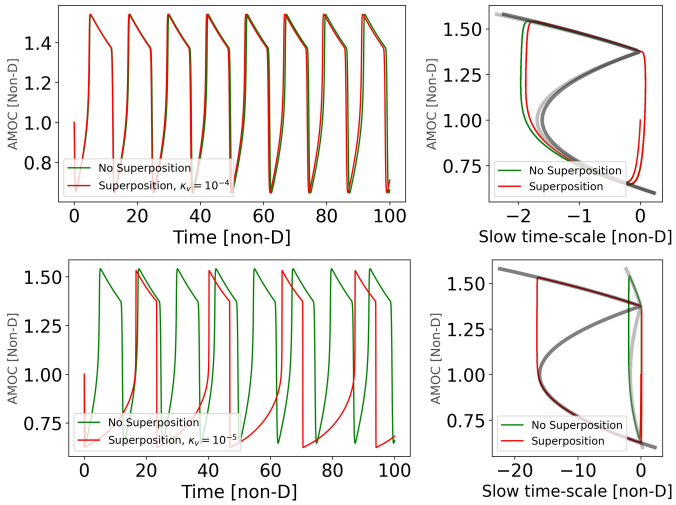

FIG. 16: Left: Box-model with runs with and without superposition, for different values of κ_v. Right: Ensuing phase spaces with and without superposition. Light gray is the slow manifold without superposition. Dark gray is with superposition.

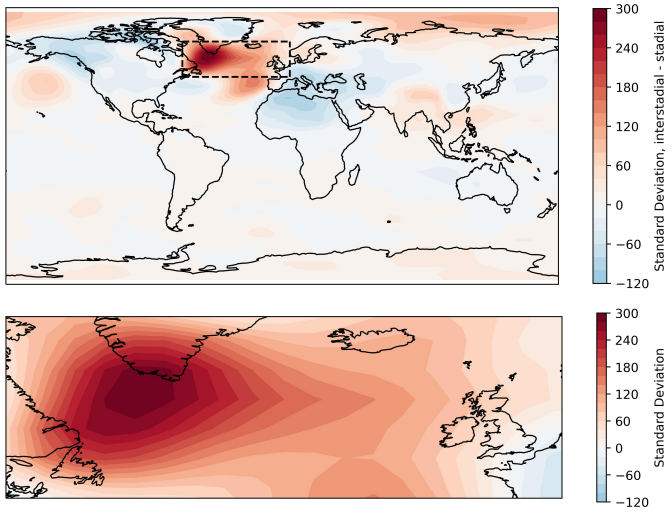

FIG. 17: Standard deviation [Pa] of sea level pressure at each point of the earth in a 48x96 grid.

Further exploration of κ_v is required.

B. Variability Analysis

In order to enhance the capabilities of our box-model, we propose the incorporation of a dynamic noise magnitude, σ, that varies based on the state. Specifically, this noise magnitude would be dependent on whether the model is in interstadial or stadial-like conditions.

By implementing higher noise in stadial conditions, we increase the chances of noise-induced transitions to the interstadial state. On the other hand, when the box-model is in interstadial conditions, we could reduce the noise magnitude in order to constrain the box-model from easily transitioning back to stadial states. This helps to maintain the box-model in a more stable, interstadial state for longer periods of time while destabilizing the stadial state, as is desired due to the lack of events and too high values of $P'(t)$ in figs. 13 and 14

Therefore, we aim to investigate whether the North Atlantic sea exhibits different levels of variability in stadial versus interstadial conditions, and if so, which one exhibits higher variability. To do this, we will analyze high temporal-resolution model data from a CCSM4 model run, using simulated data from a hundred-year period in stadial-like conditions and a hundred-year period in interstadial-like conditions. The data has a three-hour resolution and is based on a 48 by 96 grid of the world. Using the deviations in sea level pressure (PSL) as a proxy for the storminess of the region. Calculating the standard deviation of the 100-year periods, of each grid point and mapping the results on the world. The results from the stadial conditions are then subtracted from the interstadial results, and shown in fig. fig. 17.

We observe that, in general, pressure exhibits lower variability in interstadial conditions over landmasses and vice versa over oceans in the Northern Hemisphere. However, the region of very large interstadial variability in the North Atlantic ocean stands out as particularly interesting.

We see that this region of large variability exhibits higher pressure fluctuations in interstadial conditions compared to stadial conditions. This suggests that the North Atlantic sea is more prone to stormy conditions during interstadial periods in this particular region. In addition to using storminess as a proxy for noise in our box-model, we also want to investigate the relationship between noise in pressure and in temperature. We calculate the standard deviation of temperature at the 850 hPa level for each grid point in both stadial and interstadial conditions, and then subtract the stadial value from the interstadial value. The resulting data is depicted in Figure 18.

Upon examining the results, we find that temperature variability appears to be relatively constant across the entire world when comparing stadial to interstadial con-

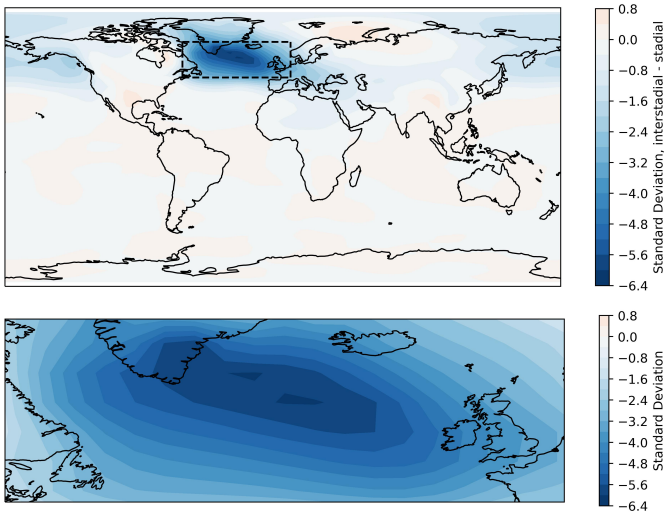

FIG. 18: Standard deviation [K] of temperature at each point of the earth in a 48x96 grid.

ditions. However in the North Atlantic ocean, we observe that temperature is actually more variable in stadial conditions than in interstadial conditions, which is the opposite of what we found for pressure. This suggests that there may be complex and possibly counteracting influences on temperature and pressure variability in this region, which we can not give physical reason for at the moment.

X. AKNOWLEDGEMENTS

The authors would like to thank Thea Quistgaard for help with optimising the code to a point that makes the Monte Carlo sampling possible, as well as loads of input and feedback with the project. Johannes Lohmann for providing code and data, discussing the analysis and giving examples of fitting routines for the forced simulations that might converge. Peter Ditlevsen for explaining and discussing the theoretical framework behind the analytical analysis, and to help formulate the idea behind the project. Jacob Osman, for help with statistics, specifically the scatter plots. Johann Severin and Albert Sneppen for discussing the statistical analysis. Anders Svenson for talks about the impact of volcanoes on the DO cycle. Julius Beiergaard for numerical analysis scheme and fitting routines. Of course, a heartfelt thanks go to our supervisors Guido and Sune for invaluable insights, excellent explanations, and safe steering, over the last year, on alpine peaks, in halls of Frederiksberg and in offices at Tagensvej 16.

REFERENCES

Bereiter, B. et al. “Revision of the EPICA Dome C CO $_2$ record from 800 to 600 kyr before present: Analytical bias in the EDC CO2 record”. en. In: *Geophysical Research Letters* 42.2 (Jan. 2015), pp. 542–549. DOI: 10.1002/2014GL061957.

Berglund Nils, G. B. *Noise-Induced Phenomena in Slow-Fast Dynamical Systems: : A Sample-Paths Approach*. eng. Probability and its Applications. OCLC: 1346394234. London: Springer Science+Business Media, LLC, 2010.

Bond, G. et al. “A Pervasive Millennial-Scale Cycle in North Atlantic Holocene and Glacial Climates”. en. In: *Science* 278.5341 (Nov. 1997), pp. 1257–1266. DOI: 10.1126/science.278.5341.1257.

Buizert, C. et al. “Precise interpolar phasing of abrupt climate change during the last ice age”. en. In: *Nature* 520.7549 (Apr. 2015). Number: 7549 Publisher: Nature Publishing Group, pp. 661–665. DOI: 10.1038/nature14401.

Capron, E. et al. “The anatomy of past abrupt warmings recorded in Greenland ice”. en. In: *Nature Communications* 12.1 (Apr. 2021). Number: 1 Publisher: Nature Publishing Group, p. 2106. DOI: 10.1038/s41467-021-22241-w.

Corrick, E. C. et al. “Synchronous timing of abrupt climate changes during the last glacial period”. In: *Science* 369.6506 (Aug. 2020). Publisher: American Association for the Advancement of Science, pp. 963–969. DOI: 10.1126/science.aay5538.

Dansgaard, W. et al. “Evidence for general instability of past climate from a 250-kyr ice-core record”. en. In: *Nature* 364.6434 (July 1993). Number: 6434 Publisher: Nature Publishing Group, pp. 218–220. DOI: 10.1038/364218a0.

Gent, P. R. et al. “The Community Climate System Model Version 4”. EN. In: *Journal of Climate* 24.19 (Oct. 2011). Publisher: American Meteorological Society Section: Journal of Climate, pp. 4973–4991. DOI: 10.1175/2011JCLI4083.1.

Huybers, P. “Early Pleistocene Glacial Cycles and the Integrated Summer Insolation Forcing”. In: *Science* 313.5786 (July 2006). Publisher: American Association for the Advancement of Science, pp. 508–511. DOI: 10.1126/science.1125249.

Kowalczyk, P. and P. Glendinning. “Boundary-equilibrium bifurcations in piecewise-smooth slow-fast systems”. In: *Chaos: An Interdisciplinary Journal of Nonlinear Science* 21.2 (June 2011). Publisher: American Institute of Physics, p. 023126. DOI: 10.1063/1.3596708.

Lohmann, J. and P. Ditlevsen. “Random and externally controlled occurrences of Dansgaard–Oeschger events”. English. In: *Climate of the Past* 14.5 (May 2018). Publisher: Copernicus GmbH, pp. 609–617. DOI: 10.5194/cp-14-609-2018.

Lohmann, J. and A. Svensson. “Ice core evidence for major volcanic eruptions at the onset of Dansgaard–Oeschger warming events”. English. In: *Climate of the Past* 18.9 (Sept. 2022). Publisher: Copernicus GmbH, pp. 2021–2043. DOI: 10.5194/cp-18-2021-2022.

Menviel, L. et al. “An ice–climate oscillatory framework for Dansgaard–Oeschger cycles”. en. In: *Nature Reviews Earth & Environment* 1.12 (Dec. 2020). Number: 12 Publisher: Nature Publishing Group, pp. 677–693. DOI: 10.1038/s43017-020-00106-y.

Menviel, L. et al. “Hindcasting the continuum of Dansgaard-Oeschger variability: mechanisms, patterns and timing”. English. In: *Climate of the Past* 10.1 (Jan. 2014). Publisher: Copernicus GmbH, pp. 63–77. DOI: 10.5194/cp-10-63-2014.

Mitsui, T. and M. Crucifix. “A statistical modelling study of the abrupt millennial-scale climate changes focusing on the influence of external forcings”. In: *Climate Dynamics* 48 (Apr. 2017). DOI: 10.1007/s00382-016-3235-z.

Pedro, J. B. et al. “Dansgaard-Oeschger and Heinrich event temperature anomalies in the North Atlantic set by sea ice, frontal position and thermocline structure”. en. In: *Quaternary Science Reviews* 289 (Aug. 2022), p. 107599. DOI: 10.1016/j.quascirev.2022.107599.

Pedro, J. B. et al. “Beyond the bipolar seesaw: Toward a process understanding of interhemispheric coupling”. en. In: *Quaternary Science Reviews* 192 (July 2018), pp. 27–46. DOI: 10.1016/j.quascirev.2018.05.005.

Rasmussen, S. O. et al. “A stratigraphic framework for abrupt climatic changes during the Last Glacial period based on three synchronized Greenland ice-core records: refining and extending the INTIMATE event stratigraphy”. en. In: *Quaternary Science Reviews* 106 (Dec. 2014), pp. 14–28. DOI: 10.1016/j.quascirev.2014.09.007.

Riechers, K. et al. “Orbital insolation variations, intrinsic climate variability, and Quaternary glaciations”. English. In: *Climate of the Past* 18.4 (Apr. 2022). Publisher: Copernicus GmbH, pp. 863–893. DOI: 10.5194/cp-18-863-2022.

Rohling, E. J. et al. “Controls on the East Asian monsoon during the last glacial cycle, based on comparison between Hulu Cave and polar ice-core records”. en. In: *Quaternary Science Reviews* 28.27 (Dec. 2009), pp. 3291–3302. DOI: 10.1016/j.quascirev.2009.09.007.

Schmitt, R., P. Bogden, and C. Dorman. “Evaporation Minus Precipitation and Density Fluxes for the North Atlantic”. In: *Journal of Physical Oceanography* 19 (Aug. 1989), pp. 1208–1221. DOI: 10.1175/1520-0485(1989)019<1208:EMPADF>2.0.CO;2.

Stocker, T. F. and S. J. Johnsen. “A minimum thermodynamic model for the bipolar seesaw”. en. In: *Paleoceanography* 18.4 (2003). DOI: 10.1029/2003PA000920.

Stommel, H. “Thermohaline Convection with Two Stable Regimes of Flow”. en. In: *Tellus* 13.2 (1961), pp. 224–230. DOI: 10.1111/j.2153-3490.1961.tb00079.x.

Strogatz, S. *Nonlinear dynamics and chaos: with applications to physics, biology, chemistry, and engineering*. eng. Second edition. Boca Raton, FL: CRC Press, Taylor & Francis Group, 2018.

Svensson, A. et al. “Bipolar volcanic synchronization of abrupt climate change in Greenland and Antarctic ice cores during the last glacial period”. English. In: *Climate of the Past* 16.4 (Aug. 2020). Publisher: Copernicus GmbH, pp. 1565–1580. DOI: 10.5194/cp-16-1565-2020.

Vettoretti, G. and Peltier. “Fast Physics and Slow Physics in the Nonlinear Dansgaard-Oeschger Relaxation Oscillation”. In: *Journal of Climate* 31 (Jan. 2018). DOI: 10.1175/JCLI-D-17-0559.1.

Vettoretti, G. and Peltier. “Thermohaline instability and the formation of glacial North Atlantic super polynyas at the onset of Dansgaard-Oeschger warming events”. en. In: *Geophysical Research Letters* 43.10 (2016), pp. 5336–5344. DOI: 10.1002/2016GL068891.

Vettoretti, G. et al. “Atmospheric CO2 control of spontaneous millennial-scale ice age climate oscillations”. en. In: *Nature Geoscience* 15.4 (Apr. 2022). Number: 4 Publisher: Nature Publishing Group, pp. 300–306. DOI: 10.1038/s41561-022-00920-7.

Wallace, J. M. and P. V. Hobbs. *Atmospheric science: an introductory survey*. eng. 2nd ed. International geophysics series. Amsterdam: Elsevier USA, 2006.

Name	**Symbol**	**Value**	**Unit**
pycnocline depth	D	1000.0	m
ocean vertical mixing	κ_v	1.0×10^{-4}	m^2s^{-1}
buoyancy flux e-folding time scale	τ	150.0	years
characteristic time	τ_c	166.6	years
characteristic buoyancy	b_c	0.004	ms^{-2}
characteristic buoyancy flux	B_c	3.8×10^{-10}	m^2s^{-3}
characteristic CO_2 (buoyancy units)	γ_c	0.004	ms^{-2}
characteristic volume transport	q_c	0.67	Sv
dimensional freshwater stream function y-intercept	q_0	-6.0	Sv
dimensional freshwater stream function slope	q_1	8.0	Sv
buoyancy (y-axis) adjustment parameter	b_0	0.625	[]
AMOC stream function y-intercept	ψ_0	-4.5	Sv
AMOC stream function slope	ψ_1	20.0	Sv

TABLE III: Important parameters from the supplemental of Vettoretti et al. 2022.